Climate Dynamics (1997) 13: 797–820

Climate Dynamics

East Asian winter monsoon: results from eight AMIP models

Y. Zhang[1], K. R. Sperber[1], J. S. Boyle[1], M. Dix[2], L. Ferranti[3], A. Kitoh[4], K. M. Lau[5], K. Miyakoda[6], D. Randall[7], L. Takacs[8], R. Wetherald[9]

[1]Program for Climate Model Diagnosis and Intercomparison, Lawrence Livermore National Laboratory, Livermore, CA 94550, USA
[2]Commonwealth Scientific and Industrial Research Organisation, Mordialloc, Victoria 3195, Australia
[3]European Centre for Medium-Range Weather Forecasts, Shinfield Park, Reading RG29AX, United Kingdom
[4]Meteorological Research Institute, 1-1, Nagamine, Tsukuba-shi, Ibaraki-ken, 305, Japan
[5]Goddard Space Flight Center, NASA, Code 913 Greenbelt, MD 20771, USA
[6]IMGA-CNR, Via Emilia Est 770, Modena 41100, Italy
[7]Atmospheric Sciences Department, Colorado State University, Fort Collins, Colorado 80523, USA
[8]Goddard Laboratory for Atmospheres, Goddard Space Flight Center, Greenbelt, Maryland 20771, USA
[9]Geophysical Fluid Dynamical Laboratory/NOAA, Princeton University, Princeton, New Jersey 08540, USA

Received: 10 March 1997/Accepted: 4 June 1997

Abstract. This study evaluates simulations of the East Asian winter monsoon in eight GCMs that participated in the Atmospheric Model Intercomparison Project (AMIP). In addition to validating the mean state of the winter monsoon, the cold surge and its transient properties, which includes the frequency, intensity, preferred propagation tracks, and the evolution patterns of the surges, are examined. GCM simulated temporal distribution of the Siberian high and cold surges is also discussed. Finally, the forcing of the cold surges on the tropical surface wind and convection, along with their interannual variation is analyzed. The mean state of the winter monsoon is generally portrayed well in most of the models. These include the climatological position of the Siberian high, the 200 hPa divergent center, and the large-scale wind patterns at the surface and the 200 hPa. Models display a wide range of skill in simulating the cold surge and its transient properties. In some of the models, the simulated cold surge trajectory, intensity, frequency, propagation patterns and source regions are in general agreement with those from the observed. While in others, the models cannot adequately capture these observed characteristics. The temporal distribution of the Siberian high and cold surges were realistically reproduced in most GCMs. Most models were able to simulate the effect of the cold surges on the tropical surface wind, although a few models unrealistically generated subtropical southerly wind in the mid-winter. The relationship between cold surges and the tropical convection was not satisfactorily simulated in most models. The common discrepancies in the winter monsoon simulation can be attributed to many factors. In some models, the reason is directly related to the improper location of the large-scale convective center near the western Pacific. The satisfactory simulations of the monsoon circulation and the cold surges are partly due to the topographical characteristics of the East Asian continent, i.e., the Tibetan Plateau to the west and the oceans to the east. The correct simulation of the interannual variation of the surface wind near the South China Sea (SCS) and the maritime continent is a demanding task for most of the models. This will require adequate simulations of many aspects, including tropical convection, the Siberian cold dome, the extratropical-tropical linkage, and the air-sea interaction. The discrepancies noted here furnish a guide for the continuing improvement of the winter monsoon simulations. Improved simulations will lead to an adequate delineation of the surface wind and convection near the maritime continent, which is essential for portraying the winter monsoon forcing in a coupled model.

Correspondence to: Y. Zhang
E-mail: zhang@pcmdi.llnl.gov

1 Introduction

The general characteristics of the East Asian winter monsoon have been revealed in many observational studies, especially those associated with the 1978–1979 Winter Monsoon Experiment (WMONEX). Comprehensive reviews and summaries were given by Lau and Chang (1987) and Boyle and Chen (1987). These observations have provided compelling evidence that the winter monsoon and cold surges are inherently related to the planetary and synoptic-scale disturbances in both the tropical and extratropical regions. For example, Chang et al. (1979) indicated that the effect of a strong cold surge can reach much further into the tropics than the wind could have pushed the front, resulting in freshened northerly winds near the equatorial region. Chang and Lau (1982) showed that the outbreak of cold surges forced short term changes in the Hadley and Walker circulation, the East Asian jet stream and large-scale deep convection over the equatorial western Pacific. Chang et al. (1979) and Chang and Lau (1980, 1981) have also suggested that the deep

convective heat source near the maritime continent may interact with the cold surges from the north to modify the planetary and synoptic-scale motions in the tropics and the extratropics.

Studies have also indicated the influence of cold surges on the Southern Hemisphere summer monsoon. A case presented by Davidson et al. (1983) showed that the Australian summer monsoon onset occurred after cold surge northerlies penetrated deeply across the equator during 22–26 December 1979. Shield (1985) presented further evidence linking the cold surges to monsoon development in the Southern Hemisphere. It was shown that the onset of the monsoon westerlies along 10 °S in the Indonesian region was preceded by a significant strengthening of northeasterly monsoon winds that lasted for three to four days. These evidences strongly suggest that the East Asian winter monsoon and the Southern Hemisphere summer monsoon may not be independent events.

Some recent work has brought new insight into the linkage of the winter and summer monsoon in East Asia. Zhou et al. (1996) indicated that the winter monsoon wind can induce sea surface temperature (SST) anomalies in the South China Sea (SCS) region from the late fall into spring. Tomita and Yasunari (1996) suggested that the SST anomalies around the SCS were favorable for modifying the convective activity around the maritime continent from northern winter to summer. Chu et al. (1996) suggested that the winter monsoon/ocean interaction near the SCS can influence the summer monsoon circulation in East Asia by affecting the upper ocean circulation and atmospheric diabatic heating. Based on observational evidence and model simulation, Sun and Sun (1996) suggest that a strong winter monsoon can cause a dry summer season; likewise, a weak winter monsoon may induce a wet summer season.

There has been increasing evidence suggesting that the winter monsoon is related to ENSO. For example, Ding and Krishnamurti (1987) illustrated an eastward shift of the tropical planetary-scale divergent circulation associated with the monsoon cold surges which was very similar to the shift of the divergent circulation centers between El Nino and La Nina years. Li (1990) suggested that frequent cold surges during the winter season prior to the occurrence of El Nino events may have caused the El Nino events. Zhang et al. (1997) showed the interannual variation of the monsoon wind near the SCS and the maritime continent was highly correlated ($R = 0.82$) with the Southern Oscillation Index (SOI). There is also increasing evidence suggesting that the boreal spring transition may be a very important period in determining the subsequent evolution of the monsoon as well as the interannual variability of the coupled ocean-atmosphere-land system (Webster and Yang 1992). Given that the winter monsoon-induced SST anomalies in the SCS can persist through the next autumn (Luo 1995), the oceanic "memory" of the winter monsoon can have significant impacts on the spring circulation.

Based on these observational studies, the winter monsoon is clearly an important centerpiece in the complicated interactions among different monsoon systems and the monsoon/ocean coupling near the SCS and the maritime continent. Therefore, one can hardly overexaggerate the importance of studying the winter monsoon, and the associated physical mechanisms between these interactions and between the monsoon/ENSO coupling.

The wide range of spatial and temporal scales of the atmospheric phenomena related to the winter monsoon and their interactions with the tropical oceans pose serious challenges on using simple models to tackle this problem. To use a fully coupled atmospheric-ocean model is still premature at the moment. The difficulty stems not only from problems of coupling itself, but also the lack of understanding on how the winter monsoon and cold surges are simulated in the current generation of atmospheric GCMs (AGCMs). Although model simulations of the Asian summer monsoon have been studied extensively in recent years (i.e., Barnett et al. 1989; Meehl 1994; Sperber et al. 1994; Ju and Slingo 1995, Sperber and Palmer 1996), the discussion of the winter monsoon simulations is very limited (e.g., Slingo 1997). Thus, the purpose of this study is to bridge this gap by thoroughly examining the simulation of the winter monsoon and cold surges in eight AGCMs that participated in the Atmospheric Model Intercomparison Project (AMIP).

The AMIP (Gates 1992) is a coordinated international effort to study simulations of the 1979–88 decade using atmospheric GCMs. All the simulations employed the same SST, sea ice, solar constant, and CO_2 concentration, thus enabling intercomparison of GCMs that have been integrated under standard conditions. The intercomparison of GCM simulated winter monsoon includes three main parts: (1) the mean state of the winter monsoon, (2) the cold surge and its transient properties, (3) the forcing of cold surges on the tropical surface wind and convection.

The description of the GCMs and the observed data is given in Sect. 2, followed by background and methodology in Sect. 3. Results and discussions are presented in Sect. 4, and the summary and conclusions appear in Sect. 5.

2 GCMS and observed data

High-frequency model output (once and twice daily) from AMIP simulations have been acquired from different modeling groups and stored at the Program for Climate Model Diagnosis and Intercomparison (PCMDI). The mean sea level pressure (SLP), surface air temperature, and surface wind are among the quantities necessary to describe the winter monsoon. A GCM is included in this study if at least two of these variables (one must be the surface air temperature) are available in the database. Table 1 shows the basic characteristics of the eight models whose results will be presented in this study. Further details on the dynamical formulation and physical parametrization of each model are available in Phillips (1994).

The observed data used for evaluation is the NCEP/NCAR reanalysis (Kalnay et al. 1996). This dataset has been used to provide the same derived quantities compared to those obtained from the models for the purpose of validation. The quantities include the twice-daily SLP, surface air temperature, surface wind, and

Table 1. Modeling groups participated in this study

Model	AMIP representative	Resolution	Comments
Commonwealth Scientific and Industrial Research Organisation, Australia (CSIRO)	M. Dix	R21, L9	
Colorado State University (CSU)	D. Randall	$4^\circ \times 5^\circ$, L17	
Dynamical Extended-Range Forecasting (DERF)	K. Miyakoda	T42, L18	Daily output
European Centre for Medium-range Weather Forecasts (ECMWF)	L. Ferranti	T42, L19	
Geophysical Fluid Dynamic Laboratory (GFDL)	R. Wetherald	R30, L14	Daily output; PMSL not available
Goddard Laboratory for Atmospheres (GLA)	W. Lau	$4^\circ \times 5^\circ$, L17	
Goddard Space Flight Center (GSFC)	L. Takacs	$4^\circ \times 5^\circ$, L20	
Meteorological Research Insitute (MRI)	A. Kitoh	$4^\circ \times 5^\circ$, L15	Surface wind not available

200 hPa velocity potential and wind. This data was assimilated by a "frozen" state-of-the-art analysis/forecast system, and was free from human induced "climate change". Also, this dynamically consistent reanalysis offers adequate horizontal ($2.5^\circ \times 2.5^\circ$) and vertical resolution (17 levels) for the study of the winter monsoon.

3 Background

This section is intended to provide a brief background of the winter monsoon and cold surges, and to explain the rational of choosing the variables for this study.

The key driving force for the winter monsoon, similar to its summer counterpart, is the available potential energy generated by the differential heating between land and sea. During the winter season, the main heating source is situated over the maritime continent. The latent heat release associated with intense convective precipitation fuels the gigantic planetary-scale overturning in the meridional direction. The 200 hPa velocity potential minimum near the equatorial western Pacific, which represents the divergent component of the motion, is a manifestation of the tropical convection. To the far north of this convective center lies a very strong cold dome near the Siberian region. The intensity of this cold dome is maintained by strong radiative cooling, large-scale descending motion, and persistent cold air advection throughout the troposphere (Ding and Krishnamurti 1987). This planetary-scale descending motion, and the ascending motion near the maritime continent form a strong local Hadley cell in the East Asian region.

Closely connected to the Hadley circulation is the East Asian westerly jet near 200 hPa. This jet is associated with intense baroclinicity, large vertical wind shear and strong cold air advection. The Coriolis torque exerted on the ageostrophic southerly wind in the upper branch of the Hadley cell contributes to the maintenance of this jet. The dominant surface feature of the winter monsoon is the Siberian high. This pressure system covers the entire East Asian continent and yields northeasterly flow over a large part of Asia. The associated anticyclonic surface wind over the continent is primarily attributed to this quasi-stationary system. The intensity of this high pressure is inherently related to other planetary-scale features of the winter monsoon.

The Tibetan Plateau plays a crucial role in forming the circulation patterns of the winter monsoon. The Plateau not only largely controls the flow configuration in the lower troposphere, but also greatly influences the thermally direct Hadley cell and the 200 hPa jet stream (Murakami 1987). The huge zonally oriented massif of extremely high elevation also acts as a natural barrier for the cold air near the Siberian region. The cold air damming effect is important for the build-up of the Siberian high and for the outbreak of the extremely cold air that spreads along the eastern edge of the Plateau (Yeh and Gao 1979; Luo 1992).

Cold surges are the most important transient disturbances embedded within the mean monsoon circulation. The occurrence of a cold surge is characterized by a southward movement of a surface anticyclone and an associated abrupt surface air temperature decrease in the affected regions. The typical scenario of a cold air outbreak is as follows: the Siberian high and the coastal trough reach a certain intensity. Further west over the continent, an upper-level short wave undergoes strong developments as it moves eastward. Eventually, the short wave develops into a major trough and replaces the old quasi-stationary coastal trough. During this process, a surface anticyclone moves southward and a cold surge occurs (Staff members of Academia Sinica 1958).

The build-up and maintenance of the Siberian high pressure is a necessary condition for the occurrence of cold surges. In the extratropical regions, the surface wind is primarily dominated by the quasi-stationary Siberian pressure. Despite the shallowness of the cold air near the tropical region, the cumulative effects of cold surges dominate the northerly surface wind near the SCS and the maritime continent (Zhang et al. 1997). The Siberian high and the cold surge are the two most characteristic weather phenomena of the winter monsoon, and both will be investigated in this study.

In examining the mean monsoon circulation, the East Asian regional features of SLP and surface wind, and the

200 hPa wind and velocity potential will be analyzed. To study the cold surge, we will focus on its origin, trajectory, frequency, and intensity. In addition, we will discuss the cold surge associated spatial evolution of SLP, surface air temperature and surface wind, and the temporal distribution of the Siberian high and the cold surges. The ability of the GCMs to simulate the effect of the cold surges on the surface wind near the SCS and the convection near the maritime continent, along with their interannual variation, will also be investigated.

4 Results and discussions

4.1 Mean monsoon circulation

As noted previously, the SLP, surface wind, 200 hPa wind and velocity potential are among the most representative variables of the mean monsoon circulation. These variables are readily comparable with observations, and some exhibit monsoon circulation patterns of particular interest. Except as specified, all of the climatological

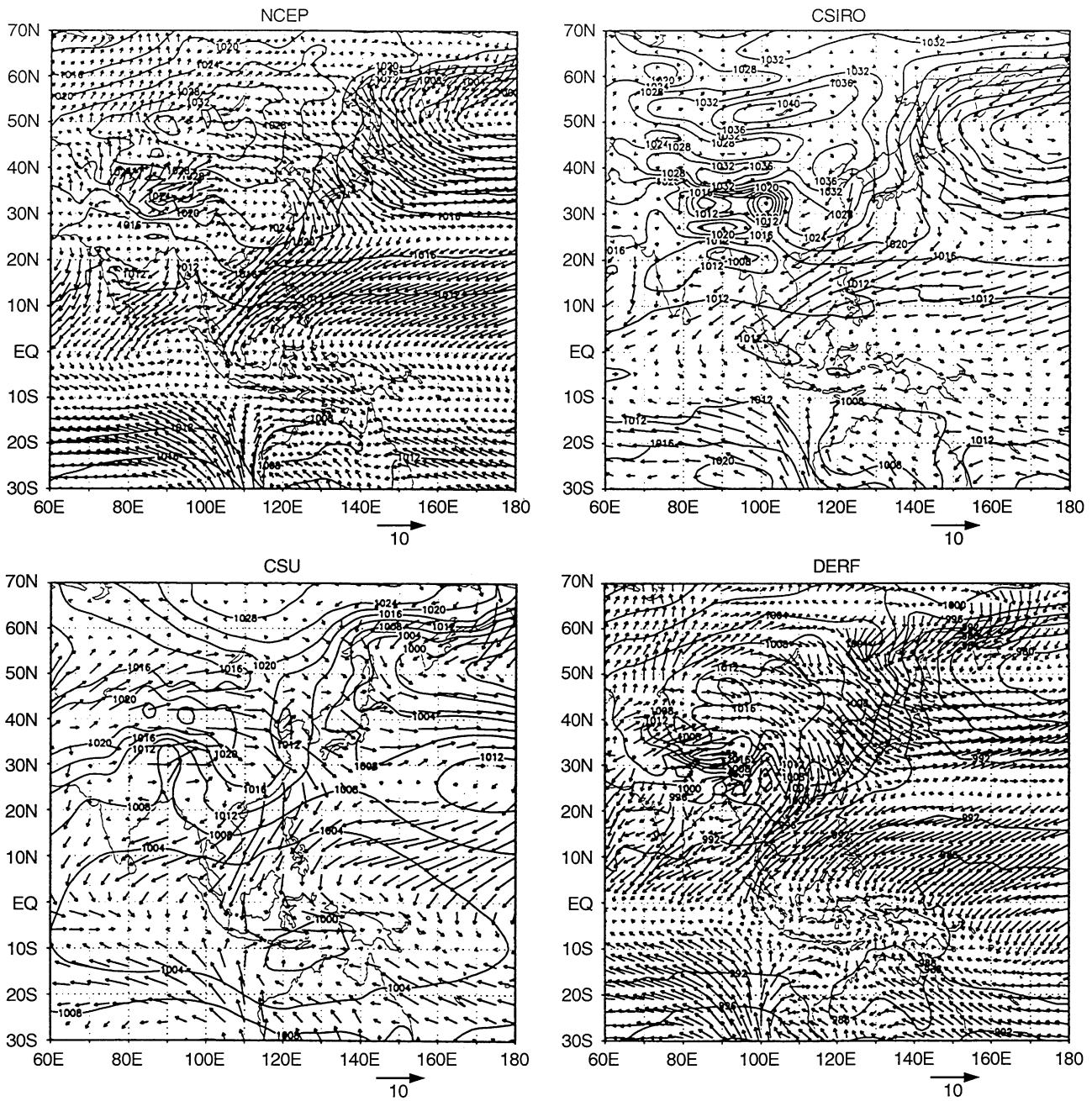

Fig. 1. The East Asian mean sea-level pressure superimposed on the surface wind averaged for the winters (DJF) of 1979/80–1987/88 from the reanalysis and the models. Units: hPa and $m\,s^{-1}$

distributions shown here, observation and simulation alike, were determined from the 9-winter-seasons (DJF) of 1979/80 to 1988/89.

4.1.1 Sea-level pressure and wind. The East Asian regional distribution of the average SLP simulated from the models is shown in Fig. 1, together with the observed pattern from the reanalysis. Most models have correctly depicted the broad features of the SLP distribution. The center position of the Siberian high, located between the northern part of the Tibetan Plateau and Lake Baikal, is well simulated in most of the models, particularly in the ECMWF and the MRI GCMs. In the GSFC, GLA and DERF models, the center is slightly displaced to the southwest compared to the observation. The CSU model fails to reproduce the closed SLP contours near the Siberian region, while the pressure field from the CSIRO is too noisy. Some of the models, such as the CSIRO, ECMWF, and MRI, simulate the intensity of the high pressure quite accurately. In the GLA and the GSFC GCMs, however, the central pressure is 7 hPa too low, and the most serious underestimate is from the CSU and DERF models, being about 20 hPa. The underestimate in the CSU model is, most likely, due to the use of

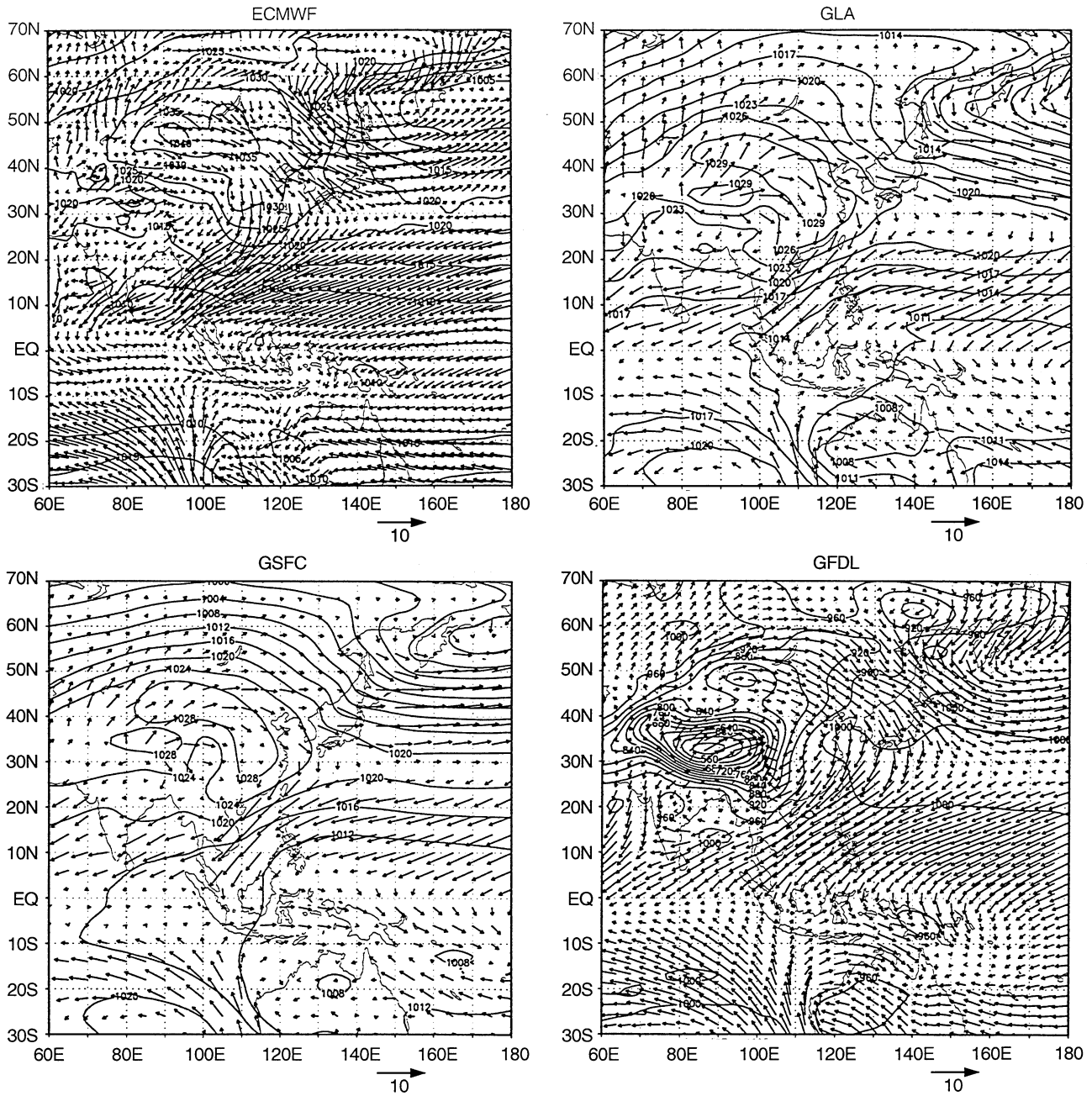

Fig. 1. (Continued on page 802)

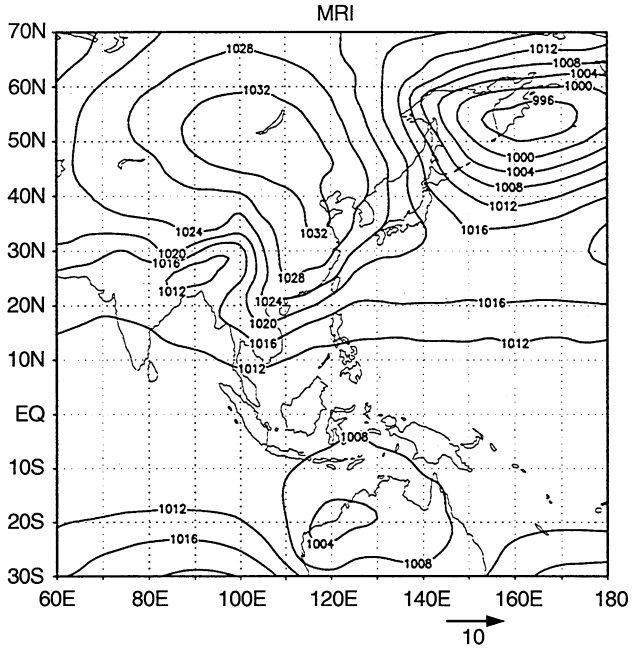

Fig. 1. (Continued)

dry-adiabatic lapse rate when reduction to sea level is performed. This is because the use of dry-adiabatic lapse rate will induce too large a thickness increment for a given pressure increment, or too little pressure increment for a given thickness increment. This will make lows appears too strong and highs too weak over elevated terrain. A test run is planned with the CSU model to confirm this conjecture.

The location of the neighboring Aleutian low is portrayed quite well in most of the models, although the GSFC and MRI GCMs displace the low pressure system to the north and northwest of the observed location, and they steepen the pressure gradient between the Siberian high and the Aleution low. The northward displacement of the Aleutian low in GSFC is due to the lack of gravity-wave drag in the model. In the new version of GSFC, the gravity-wave drag parametrization is included and the position of the Aleutian low is correctly reproduced. The improper location of the Aleutian low in the MRI model may be related to the westward displacement of the tropical convection, which will be discussed in the next section. Most of the models have reproduced the minimum central pressure to within 4 hPa of the observations, although it is 20 hPa too low in the DERF model. The systematic underestimation of the pressure field in the DERF model is believed to be due to a computational error when the AMIP output was generated.

Superimposed on the SLP field in Fig. 1 is the average surface wind. North of 30 °N, the observed wind blows anticyclonically along the north and east periphery of the Siberian high, a reflection of the quasi-stationary pressure system. South of 30 °N, where the Siberian high pressure exerts less influence, the wind maximum near the SCS can be mostly attributed to the cumulative effects of the cold surges. Another main feature of this field is that the westerly flow near Japan bifurcates. The eastward branch merges with the Aleutian low, while the southern branch joins the tradewind belt.

As was the case with the SLP, all models have reproduced the general features of the surface wind with reasonable accuracy, in particular the anticyclonic flow pattern and the bifurcation near Japan. Despite their low resolution, both GLA and GSFC reproduced the observed wind patterns, however, minor discrepancies exist in some models. The wind magnitude simulated from DERF, ECMWF, and the GFDL models were close to that from the observations, although the value from CSIRO is a little low. The quantitative difference between model simulated surface wind will be discussed further in Sect. 4.3.

4.1.2 200 hPa wind and velocity potential. Figure 2 shows the 200 hPa velocity potential from the reanalysis and the models. The observed center of minimum velocity potential, located near the equatorial western Pacific, represents the strong convective heat source. To the northwest of this tropical convection, a tongue of maximum velocity potential spreads from North Africa to the East Asian coastal region. The steepened gradient between these regions indicates the extensive upper-level divergent outflow from the center of the convection into northeastern China, the India Peninsula, and the Arabian Sea. This thermally direct overturning is most intense along the 120 °E longitude line where the gradient of velocity potential is the strongest. The strong upper-level divergent flow is associated with a convergent flow in the lower troposphere. This is indicated from the velocity potential at the 850 hPa (not shown) where the maximum center is located directly underneath the minimum center of the 200 hPa, indicating a reversal of the divergent flow from the upper to the lower troposphere.

Most of the models were able to realistically depict the location of the major heating source near the maritime continent, which is, to a large extent, associated with the warm pool SSTs. The location of the minimum center from the CSIRO, CSU, and ECMWF models is close to that from the reanalysis, although those from the DERF, GLA and GFDL models are shifted slightly to the southeast. The GSFC model, however, has placed the minimum center of velocity potential near 180 °E, which is too far eastward from the observed location. The minimum center from the MRI model is located to the west of the observed location.

The southeastward displacement of the velocity potential in the GSFC is linked to the sub-grid scale convective heating and cloud/radiative feedback process. In this version of the model, the cloud cover was unsatisfactory when compared with observed data (Takacs and Suarez 1996). In a subsequent version of the model, much work has gone into improving the cloud forcing and correcting the dry bias in the tropical atmosphere. As a result, the velocity potential in the new version of the GSFC model has been significantly improved. The westward shift of the convection in the MRI model is related to the cumulus parametrization scheme of the model. The convective scheme tends to produce more precipitation over the land

than over the oceans. As a result, the simulated precipitation is confined in the maritime continent. This has naturally displaced the center minimum of velocity potential westward relative to observations.

The tongue of maximum velocity potential to the northwest of the maritime continent has also been reproduced by most of the models. Several models, such as CSU, GLA, GSFC, and MRI, generated a maximum center of velocity potential near the East Asian continent, which may have helped to enhance the gradient of velocity potential near the southeast coast of China. Despite this, none of the models were able to reproduce the gradient near Southeast Asia as strong as that from the reanalysis, although the gradient from ECMWF, CSIRO, CSU and MRI models were most realistic. In the DERF, GLA, GFDL and GSFC models, the strongest gradient near the SCS is shifted toward the maritime continent which is related to the southeastward displacement of the velocity potential center. In the GSFC model, the southeastward displacement of the velocity potential center over the dateline resulted in the weakening of gradient over the entire Southeast Asia.

Figure 2 also presents the 200 hPa wind. As mentioned before, the intensity of the East Asian jet stream is directly linked to the intensity of the Hadley cell and the convective activity near the maritime continent. The reanalysis indicates an intense confluence near the jet entrance region from about 90 °E to 120 °E. The northwesterly wind is associated with strong cold air advection which enhances the horizontal temperature gradient. The divergent outflow from the convective center near the western Pacific generates southwesterlies which serves to increase the meridional temperature gradient, and contributes to the maintenance of the jet by means of Coriolis torque acceleration.

All models have correctly simulated the observed location of the jet core and the confluence and diffluence patterns near the jet entrance and exit regions, although the eastward extension of the jet varies among the models. The intensity of the jet displays a large variation among the simulations as indicated in Table 2. The observed zonal wind is approximately 70.0 m/s, but most of the models (with the exception of the CSU, ECMWF, and MRI) underestimate the jet intensity. In the CSU, ECMWF, and MRI models, the velocity potential center is correctly reproduced. As a result, the regional gradient of velocity potential near the SCS and the intensity of the local Hadley cell are simulated well. These factors have contributed to the more realistic simulation of the jet intensity. The CSIRO model is the only one that correctly simulated the location of the velocity potential center although it fails to describe the jet intensity. This failure is unlikely to be related to the location of the convection. The magnitude of the wind at other levels and the amplitude of the surface temperature are all weak in the CSIRO model. The other models tend to underestimate the jet intensity about 10.0 m/s. The inadequate delineation of the Hadley cell intensity and the southerly ageostrophic

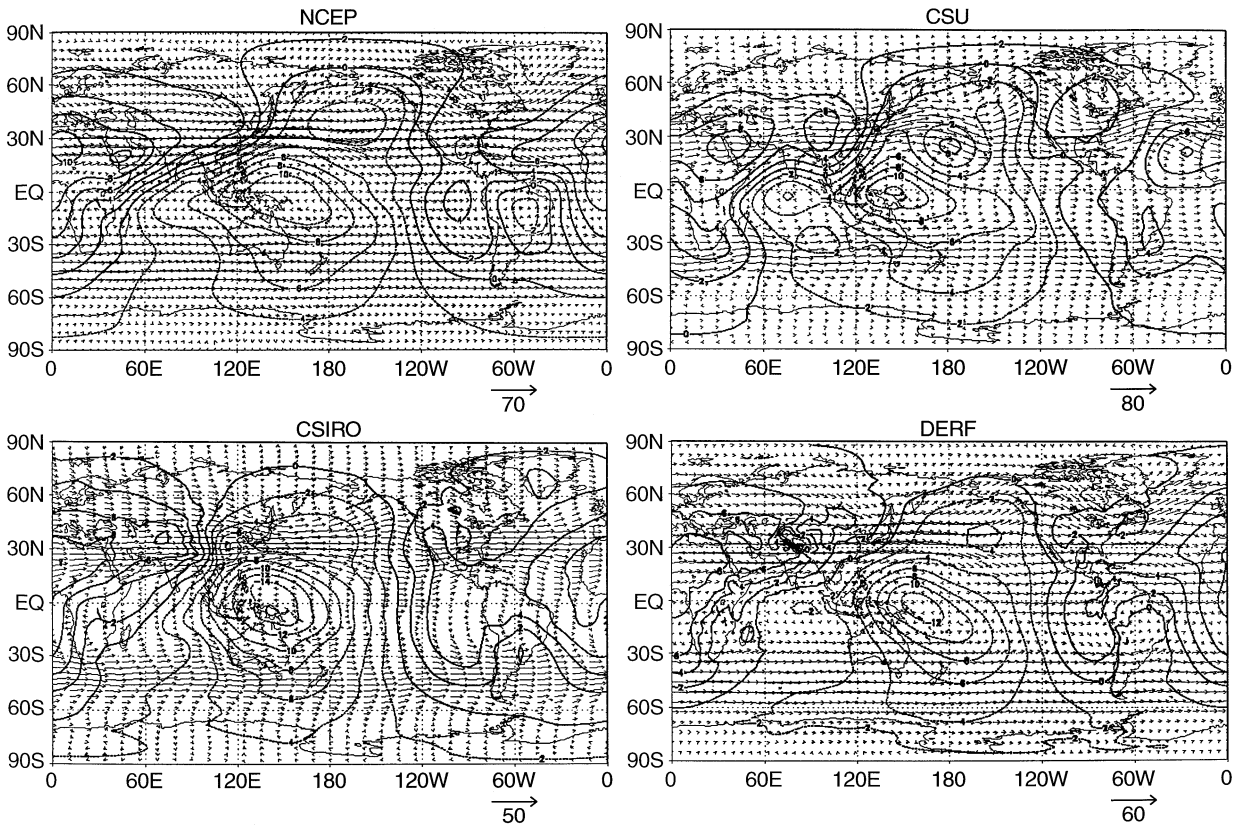

Fig. 2. The 200 hPa velocity potential superimposed on the 200 hPa wind averaged for the winters (DJF) of 1979/80–1987/88 from the reanalysis and the models. Units: $10^6\ m^2\ s^{-1}$ and $m\ s^{-1}$

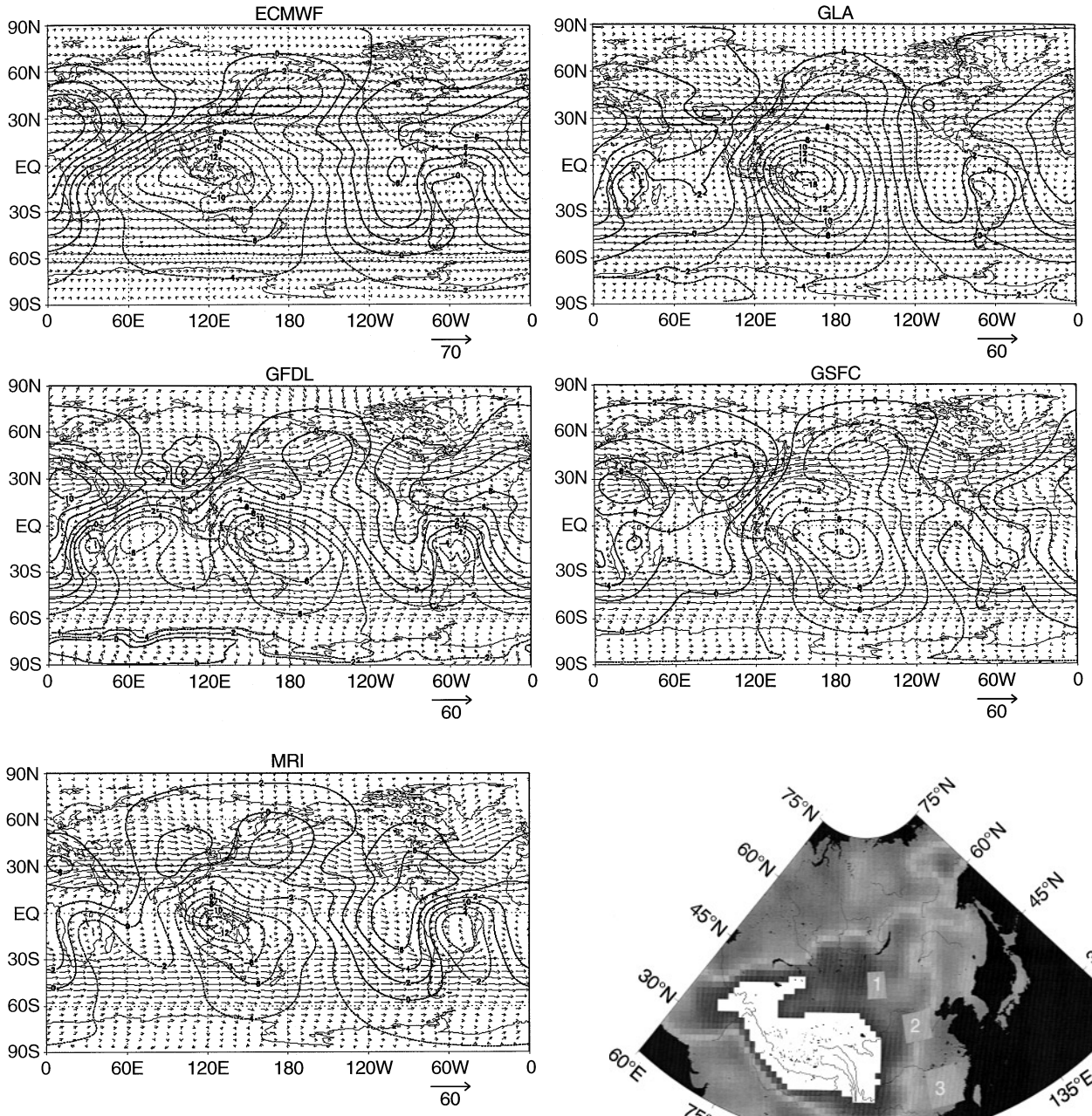

Fig. 2. (Continued)

Fig. 3. Selected sub-areas for cold surge identification in the East Asian region

wind related to the eastward deviation of the velocity potential center can be attributed to the underestimate of the jet intensity in these models.

4.2 Cold surges

Many cold surge definitions can be found in the literature. A summary of the often-used definitions is given in Boyle and Chen (1987). Some of the cold surges are purposely defined for the convenience of weather forecasting. Definitions vary depending on regions of interest. For example, cold surges defined over the SCS may have nothing to do with cold surges defined near Korea. The following definition is based on variables averaged over three regions (region 1, 2, and 3) shown in Fig. 3.

1. A cold surge occurs when, (a) a surface anticyclone is identified (criteria in Zhang and Wang 1997) near region 1. The SLP at the anticyclone center must be greater than 1035 hPa, *and* (b) during the movement of this surface anticyclone, the 24–48 h surface air temperature decrease must exceed 9 °C in region 2, *or* 6 °C in region 3.

2. A cold surge ends when, (a) a negative pressure tendency at the anticyclone center has persisted for 24 h

Table 2. Intensity of the East Asian jet (winter averaged 200 hPa zonal wind for 30 °N–35 °N, 130 °E–150 °E from 1979/80 to 1987/88)

	NCEP	CSIRO	CSU	DERF	ECMWF	GFDL	GLA	GSFC	MRI
u-wind (m/sec)	70.9	52.5	71.6	59.5	69.3	58.3	57.0	60.6	64.7

and the central pressure is less than 1025 hPa, *and* (b) a positive surface temperature trend is found over 50% of the grid points over the bulk of the East Asian continent (102.5 °E–117.5 °E, 25 °N–50 °N).

This definition reproduces the cold surge statistics that agree with the *in situ* observation from the Beijing Meteorological Center (Zhang et al. 1997). If a cold surge is associated with at least a 10 °C temperature decrease and a 4 $m\,s^{-1}$ northerly wind in region 3, then it is defined to be a strong cold surge.

Physical values in this section are chosen to delineate the characteristics of the cold surges and related transient behaviors. Comparisons of these values between observations and the models revealed some in depth ability of the models to portray cold surges and the associated transient activities as discussed fully below.

4.2.1 Temporal variation of surface air temperature. According to the cold surge definition, once a surface anticyclone is found to be moving southeastward from the source regions, the required temperature decrease in either region 2 or region 3 (see Fig. 3) will qualify the disturbance to be a cold surge. The observed and simulated time series of temperature changes from November 1987 to March 1988 are shown in Fig. 4. The observed time series illustrates how quickly the temperature can drop in a short period of time, and it demonstrates the southward propagation of the temperature decrease. Many high-frequency temperature pulses are embedded within the seasonal variation. On average, the temperature varies from −30 °C in region 1 to 25 °C in region 3. One of the strongest cold surges ever recorded occurred on 26 November 1987, during which the maximum surface pressure exceeded 1081 hPa. This event is associated with the most drastic temperature drop in region 2 and region 3.

While we do not expect a one-to-one correspondence in surge activity between the models and observations, the model simulated statistics of the temperature variation and cold surges are expected to be close to those from the observations. In broad terms the models have correctly simulated the general features of the surface air temperature in these three regions, which include the pattern of seasonal variation, the average amplitude of the surge-related temperature pulses, and the southward propagation of the pulses. Although the DERF and GLA models overestimate region 1 temperature by about 10 °C, the rest of the models simulate the temperature magnitude fairly well in all three regions. The number of surge-related temperature pulses, however, is less in most of the model simulations than the observation. The average amplitude of the simulated pulses is generally smaller than what has been observed. In the GLA simulation, the warmer surface temperature is due to the underestimation of cold air advection from the polar regions. In this version of the GLA GCM, the stationary waves have been displaced northward and the jet stream is more zonal than observed. As a result, the surface anticyclones are less well developed. This problem is corrected by the inclusion of the gravity wave drag in the latest version of the model.

The observed and model simulated region 1 SLP (not shown) have been compared with their respective temperature series in Fig. 3. In most cases, the SLP maxima coincide with region 1 temperature minima and the subsequent southward propagation of the minima, indicating the occurrences of cold surge.

The above comparison of the temperature and SLP has been limited to one season. Similar relationship between temperatures in the three regions also occur in the rest of the winter seasons.

4.2.2 Cold surge statistics and propagation pattern. Using data for the winters of 1979/80–1987/88, we have identified cold surges from the observations and models. Table 3 gives the average frequency and intensity of surges and strong surges, and their durations simulated from all GCMs, along with those from the reanalysis.

The reanalysis indicates there is on average 12 cold surges per year, and the cold surge frequency ranges from 5 events/year for the CSIRO model, to 13 events/year for the GSFC model. The consensus of all models is approximately 9 events/year. The simulated cold surge frequencies are determined by the regional anticyclone frequencies and surface temperature variations. The low surge frequency in the DERF and CSU model is consistent with the small temperature variation indicated in Fig. 4; likewise, the high frequency in the GSFC model is associated with the large temperature variation in the model. The average intensity of the cold surges, measured by the maximum SLP in the anticyclone center, is 1053 hPa from the reanalysis. The simulated intensities are close to the observed. The average intensity of all the models is approximately 1050 hPa.

The observed frequency of strong cold surges is three events/year. The simulated frequency ranges from one event/year to six events/year and has an average of approximately three events/year. The simulated intensities of the strong cold surges are in general agreement with that from the reanalysis. The SLP magnitude ranges from 1054 hPa to 1060 hPa.

The lifetime of the observed cold surges is between 5 to 14 days. The simulated cold surge duration generally agrees with this range, but has a systematic deviation toward the lower end. The largest deviation occurs in the CSIRO model, where the duration range is only 3–9 days.

The trajectories of the surface anticyclone center associated with the cold surges from the reanalysis and models are shown in Fig. 5. The circles indicate the origins of the high-pressure centers and the squares denote the termination points. The trajectories from the reanalysis indicated that cold surges tend to originate from two distinct regions. The first is located northwest of Lake Baikal near 95 °E–105 °E, 45 °N–60 °N, and the second is to the north

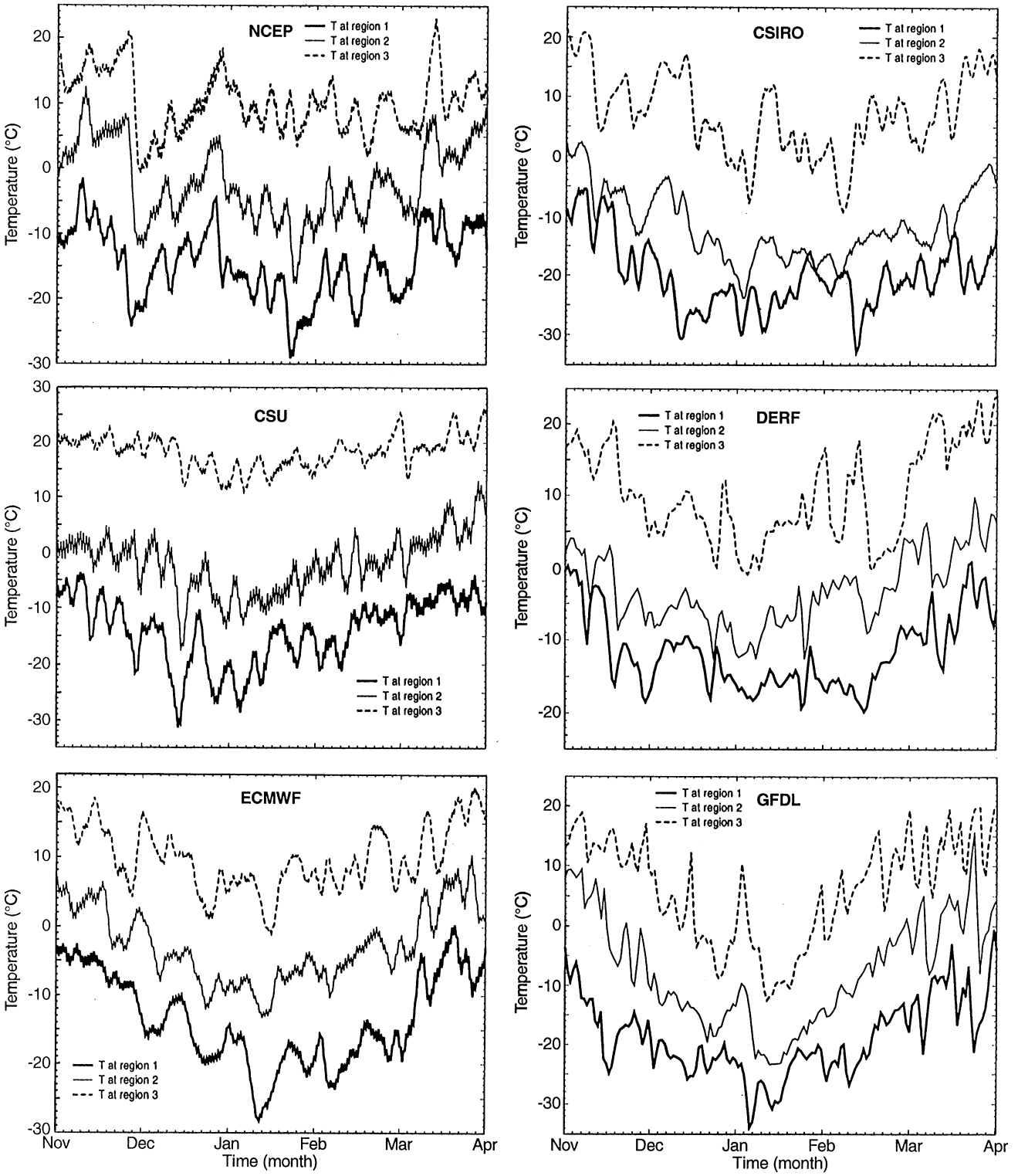

Fig. 4. Twice daily (daily for *GFDL* and *DERF*) time series of surface air temperature over regions 1, 2 and 3 from November of 1987 to March of 1988 for the reanalysis and the models. A five-point running average has been applied. Unit: °C

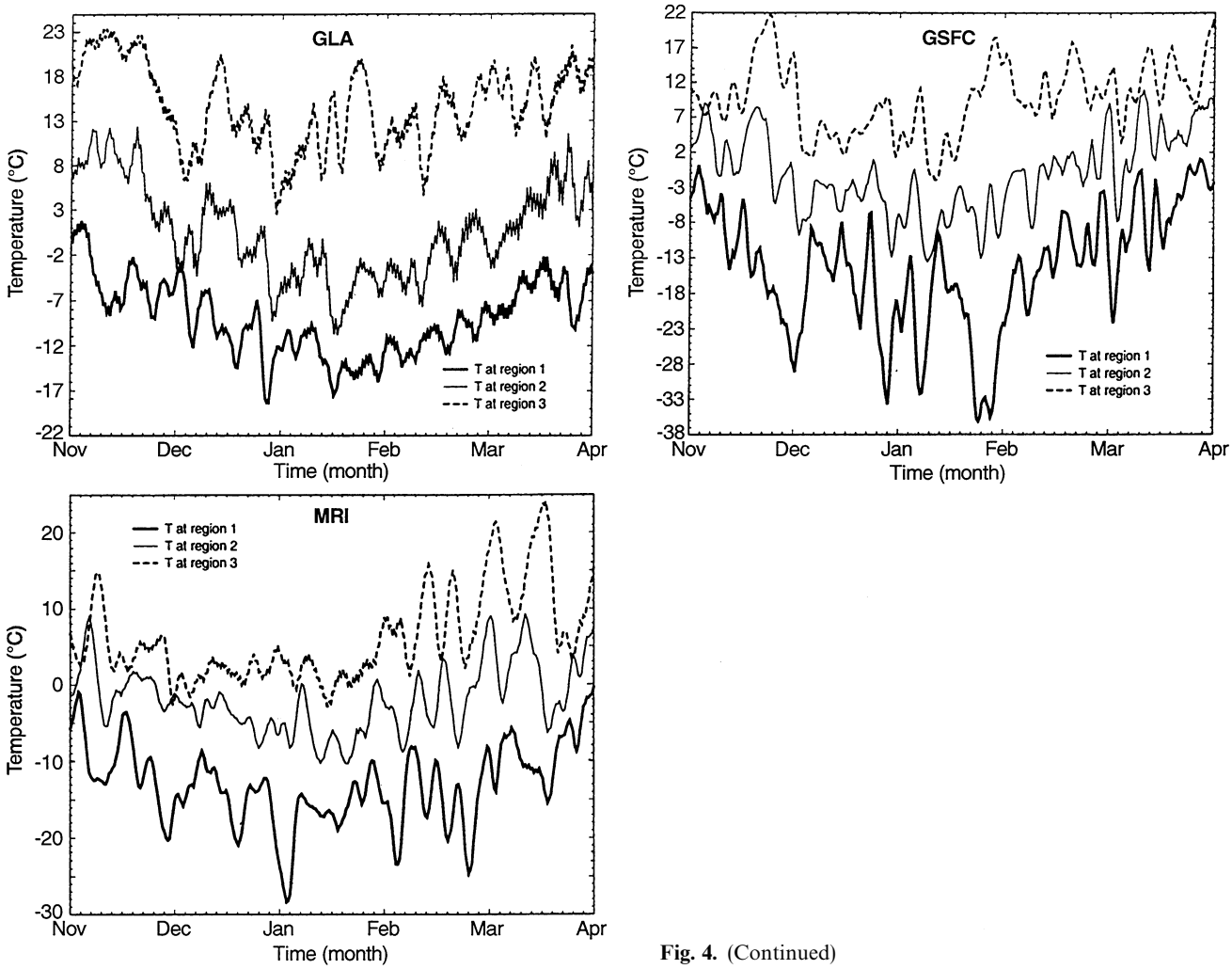

Fig. 4. (Continued)

Table 3. Model simulated East Asian cold surge statistics (1979/80–1987/88)

	*Events/year	SLP intensity (hPa)	# of intense events/year	SLP intensity (hPa)	Duration range of all cold surges
NCEP	12	1047	3	1054	5–14 days
CSIRO	5	1051	2	1057	3–9 days
CSU	9	1052	1	1054	4–10 days
DERF	7	1051	1	1060	6–11 days
ECMWF	12	1049	2	1057	5–13 days
GFDL	9	1022 (Ps)	3	1027 (Ps)	6–14 days
GLA	9	1047	2	1055	3–10 days
GSFC	13	1049	6	1054	4–11 days
MRI	9	1051	4	1054	4–12 days

of Lake Balkhash near 75 °E–90 °E, 52 °N–60 °N. All surges propagate southward or southeastward over eastern China. Some end in the East China Sea and the coastal regions, while others propagate further south.

The propagation pattern simulated from most GCMs is consistent with that from the reanalysis. The orientation of the trajectories and ending regions of the surface anticyclones typically agree with those from the observations. However, there are certain features that the models fail to capture. The two source regions of the surface anticyclones are not as distinct as those from the reanalysis. In fact, the anticyclones originate along the northwest periphery of the defined region in most of the models. The most serious failures occur in the DERF and CSIRO models. Both models underestimated the average surge frequency, and they cannot adequately portray the cold

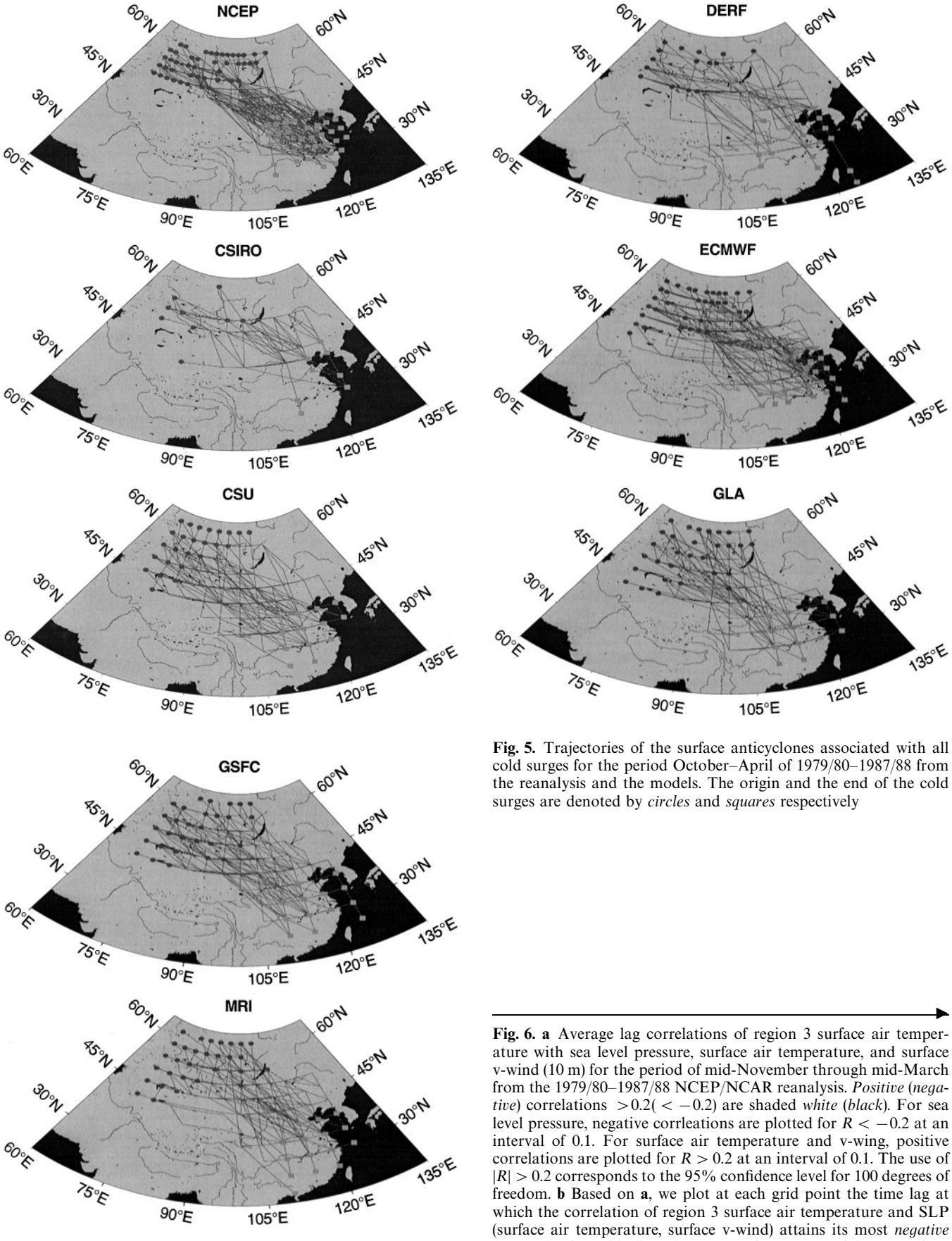

Fig. 5. Trajectories of the surface anticyclones associated with all cold surges for the period October–April of 1979/80–1987/88 from the reanalysis and the models. The origin and the end of the cold surges are denoted by *circles* and *squares* respectively

Fig. 6. a Average lag correlations of region 3 surface air temperature with sea level pressure, surface air temperature, and surface v-wind (10 m) for the period of mid-November through mid-March from the 1979/80–1987/88 NCEP/NCAR reanalysis. *Positive* (*negative*) correlations $>0.2(<-0.2)$ are shaded *white* (*black*). For sea level pressure, negative corrleations are plotted for $R<-0.2$ at an interval of 0.1. For surface air temperature and v-wing, positive correlations are plotted for $R>0.2$ at an interval of 0.1. The use of $|R|>0.2$ corresponds to the 95% confidence level for 100 degrees of freedom. **b** Based on **a**, we plot at each grid point the time lag at which the correlation of region 3 surface air temperature and SLP (surface air temperature, surface v-wind) attains its most *negative* (*positive*) value. This gives the propagation pattern of the anomalous SLP, temperature, and meridional wind during cold surges

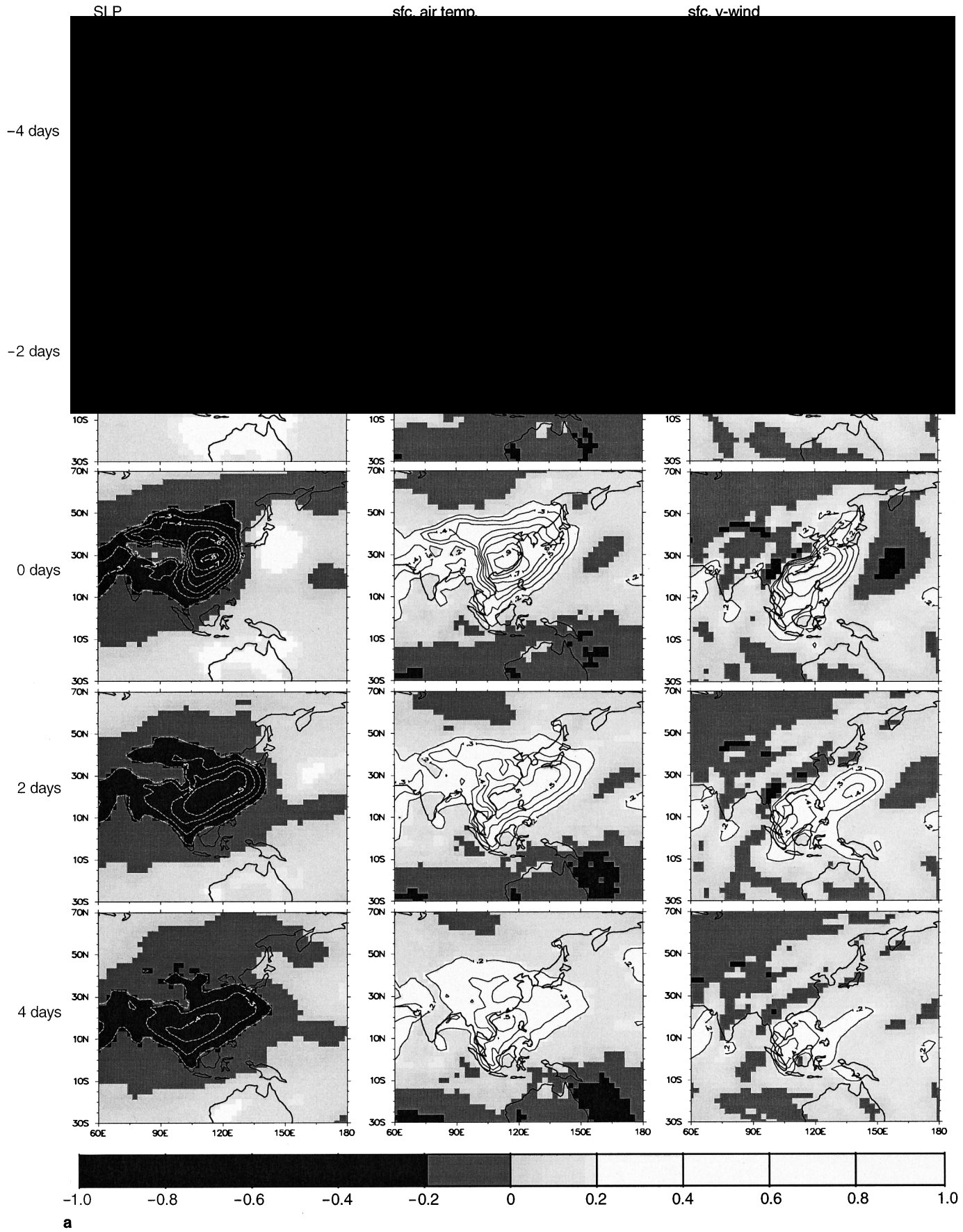
SLP
sfc. air temp.
sfc. v-wind
−4 days
−2 days
0 days
2 days
4 days
10S
30S
70N
50N
30N
10N
10S
30S
60E
90E
120E
150E
180
−1.0
−0.8
−0.6
−0.4
−0.2
0
0.2
0.4
0.6
0.8
1.0
a

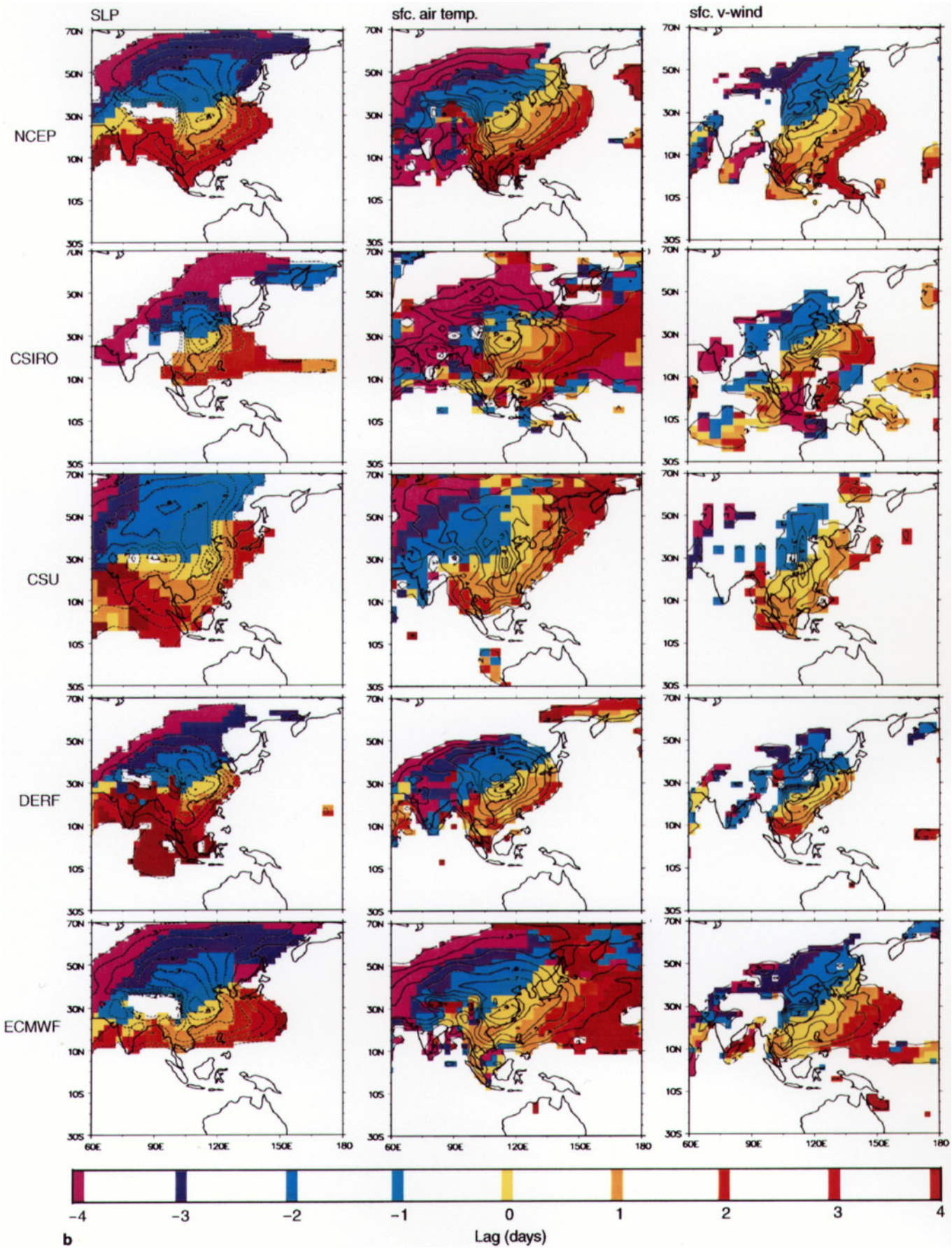

Fig. 6. (Continued)

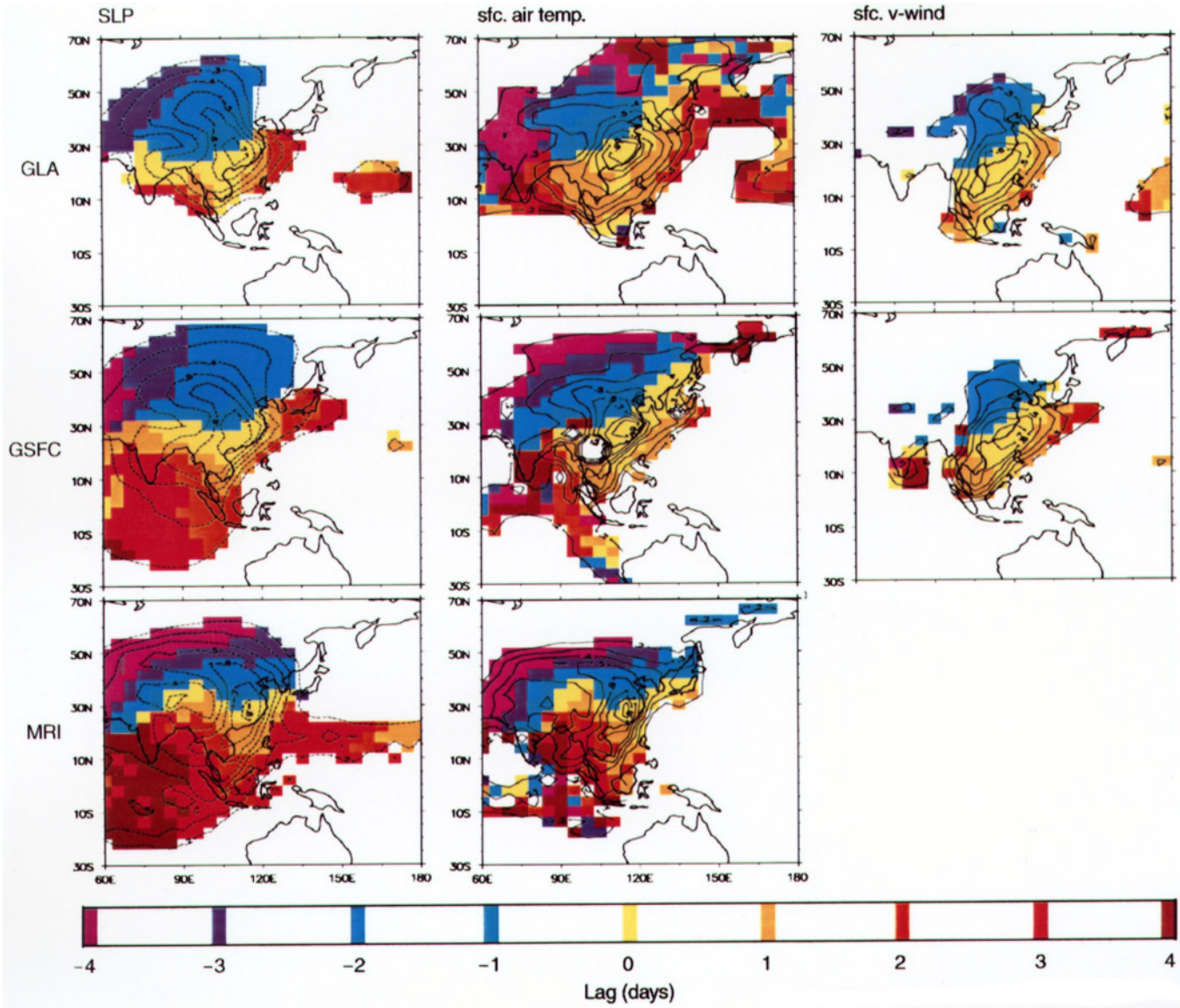

Fig. 6. (Continued)

surge trajectories. Notice that model simulated trajectories are more diffuse than those from the observed. We suspect this may be due to the relative lower model resolutions comparing to the observation.

Although the trajectories shown in Fig. 5 provide the general propagation patterns, origin, and ending of cold surges, the effects of cold surges can reach farther eastward and southward. This is illustrated in Fig. 6a and b, which show lag correlations of region 3 temperature with the SLP, temperature, and surface meridional wind from the reanalysis and from all the GCM simulations. In Fig. 6a, the average correlation at each lag from all nine winters is calculated. Given that a cold surge is associated with a temperature decrease the sign convention is such that: (1) a negative correlation with SLP indicates high pressure, (2) a positive auto-correlation with surface air temperature indicates low temperature, and (3) a positive correlation with the meridional wind indicates enhanced northerlies. Correlations for $|r| > 0.2$ are contoured. This corresponds to the 95% confidence level for 100 independent time samples (which is a conservative estimate of the degree of freedom given 120 days of data for each of the nine winters are used). For the sake of brevity, we do not show the lag correlations from odd days.

For the reanalysis, Fig. 6a reveals the following observational propagation pattern of the three fields: prior to the outbreak of the cold surges, on approximately day -4, there are temperature decreases between Siberia and the northern part of the Tibetan Plateau. This is associated with the intensification of the Siberian high and moderate increases in the northerly wind. On day -2, the magnitude of the correlation coefficient increases in all three fields, and the centers move southeastward. At the

same time, the northerly wind region has expanded substantially around the northeast coastal regions, which indicates that the majority of the cold surge outbreaks occurs at this time. On day 0, the center maxima (or minimum) in the three fields, located near region 3, continue to intensify. After day 0, the centers continue southeastward although the magnitude of the correlations decreases. From day +2 to day +4, the correlation coefficients further decrease and slowly diminish near the western Pacific. The eastward extent of the fields reaches to 150°E, and the southward stretches to 10°S. Consistent with the trajectory analysis, the lag correlations also indicate the northwest to southeast propagation of the cold surges. More importantly, it depicts the spatial domain over which cold surges can have an affect.

The propagation characteristics from the reanalysis in Fig. 6a, are summarized in Fig. 6b, along with the results from the simulations. The summary diagrams are generated from the lag correlations calculated from day −4 to day 4. For example, in the case of the region 3 temperature and SLP correlation in Fig. 6a, at each grid point we plot in Fig. 6b the time lag at which the correlation attains its most negative value (which indicates the strongest association of high pressure with low temperature in region 3). Thus, the spatial-temporal evolution of the correlations can be summarized in one plot. Sperber et al. (1997) demonstrated the usefulness of this technique for showing the propagation characteristics of the Madden-Julian Oscillation.

As in the case of cold-surge trajectory, the propagation characteristics in the three fields simulated from all GCMs tend to agree with those from the reanalysis. In all the models, a decrease of temperature in region 3 at day 0 is associated with a decrease of temperature and an increase of SLP near Siberia that was first noticed on day −4 to day −3. The maximum coefficient centers then moved southeastward, and slowly diminish near the western Pacific around day +2 to day +4, which is consistent with the reanalysis.

The models also exhibit discrepancies to varying degrees as compared to the observations. For example, the cold-surge-affected regions can be very different between models and observations. The coefficient pattern of the SLP in the CSU model during day −2 to day −1 stretches too far northward and the extent is much larger than the observed. This is also true in the GSFC model. A similar bias occurs in the SLP field from the MRI model during day +2 to day +4. A shift of a few degrees in the variation pattern is not unusual in most of the models. The most serious discrepancy is, however, the underestimation of the spatial extent influenced by the cold surges. This happened in the SLP correlations from the CSIRO, GLA and DERF models, and in the meridional wind from the DERF model, where both the southern and eastern extent are limited to within less than ten degrees as compared to the observation. The smaller spatial extent in the GLA model is likely due to the bias of the stationary wave simulations discussed previously. The physics behind the discrepancies in the rest of the models is not clear, and should be further examined and corrected in each model.

4.2.3 Temporal distribution of cold surges and Siberian high. Figure 7 gives the number of days that the Siberian high central pressure is greater than 1050 hPa and the average monthly number of cold surges simulated in all the models and from the reanalysis. The intensity of the Siberian high tends to peak in December and January and is greatly influenced by variations of the solar insolation. However, the cold-surge frequency exhibits maxima in November and March. This is because the low-index flow pattern occurs most frequently during the seasonal transition periods of November and March. This pattern usually yields northwesterlies over Lake Baikal, which are highly unstable and more likely to result in the outbreak of cold surges when triggered by a short wave (Boyle 1986). Also, the surface air temperature is relatively warm during November and March. The cold air and anticyclones with modest intensity can significantly reduce the surface air temperature and satisfy the criteria for the cold surges. In order to reproduce the observed temporal distribution in both fields, the models are required to correctly simulate both the dynamical and thermodynamical quantities in the East Asian region.

Comparing model simulated results with those from the reanalysis, we found that all the models have reproduced the observed temporal variation of the Siberian high. Most of them have also correctly simulated the peaks of cold-surge frequencies in November and in March, especially the ECMWF and CSIRO models. The Siberian high frequencies were overestimated in the MRI model with the maximum value of approximately 110 days, and underestimated in the CSU model with a value of only 26 days. The reason for the underestimation in the CSU model has been discussed previously. The range of cold surge frequencies, as seen in Fig. 7, does not vary as much as in the case of the Siberian high frequencies. But the CSU model fails to depict the peak frequencies in November and in March. The general agreement between observation and most simulations suggests that the seasonal variation in the air temperature, solar insolation, and the large-scale flow patterns are portrayed well in most GCMs.

4.3 The forcing of cold surges on the tropical wind and convection

As has been discussed, one of the most significant characteristics of the cold surges is that they propagate southward and exert strong forcing on the tropical oceans. It is the cumulative effect of the southward-propagating cold surges that greatly affects the average surface wind near the SCS and the maritime continent (Boyle and Chen 1987; Zhang et al. 1997). Because the oceans primarily feel the effect of the winter monsoon through the surface wind, the correct simulation of the southward propagation of

Fig. 7. Monthly distribution of the number of days that the Siberian high exceeds 1050 hPa and cold-surge events. These variables are for the period of October–April of 1979/80–1987/88 from the reanalysis and the models. Units: number of days and events

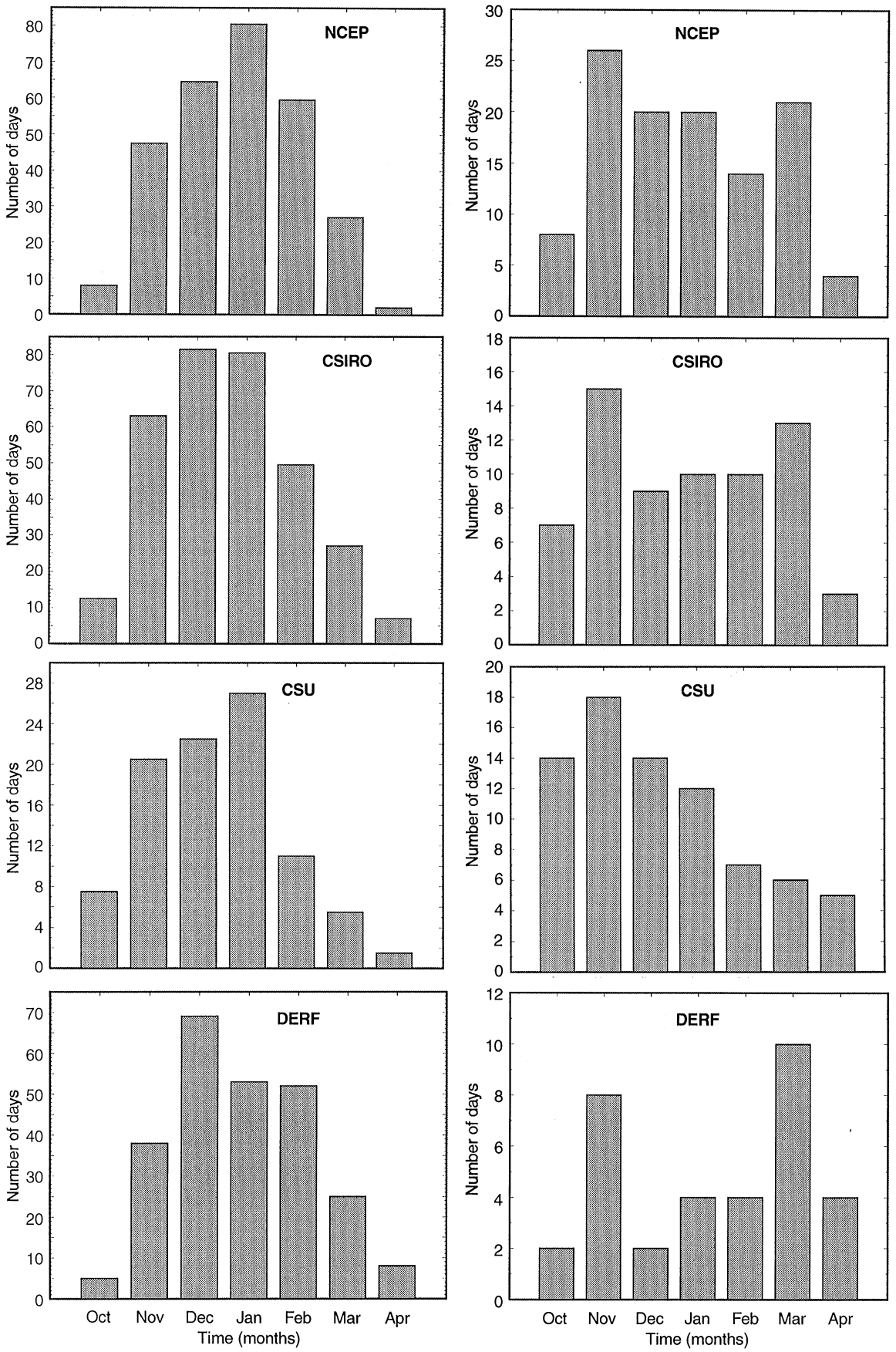
NCEP
Number of days
0
10
20
30
40
50
60
70
80
NCEP
Number of days
0
5
10
15
20
25
30
CSIRO
Number of days
0
10
20
30
40
50
60
70
80
CSIRO
Number of days
0
2
4
6
8
10
12
14
16
18
CSU
Number of days
0
4
8
12
16
20
24
28
CSU
Number of days
0
2
4
6
8
10
12
14
16
18
20
DERF
Number of days
0
10
20
30
40
50
60
70
DERF
Number of days
0
2
4
6
8
10
12
Oct
Nov
Dec
Jan
Feb
Mar
Apr
Time (months)
Oct
Nov
Dec
Jan
Feb
Mar
Apr
Time (months)

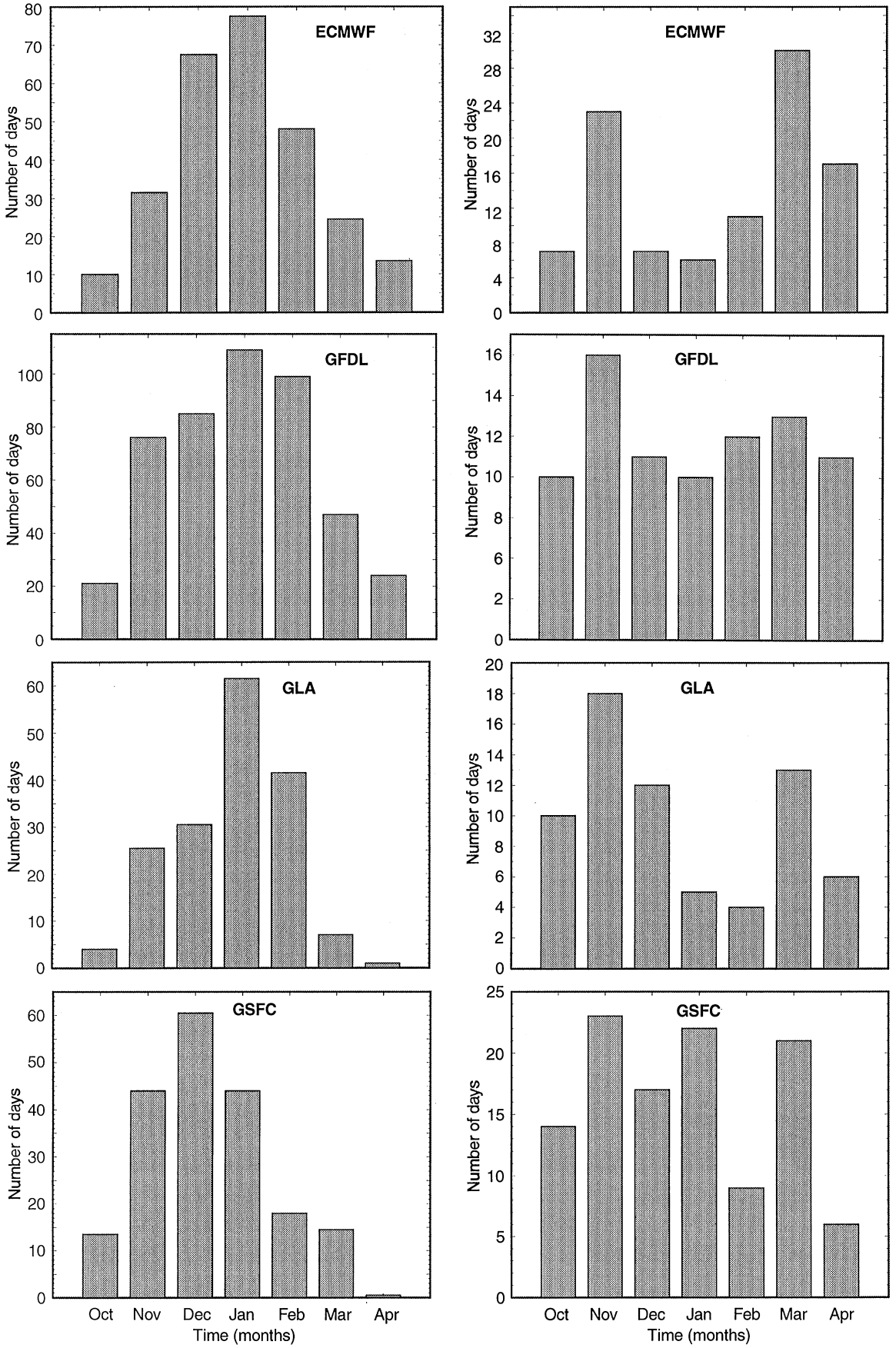

Fig. 7. (Continued)

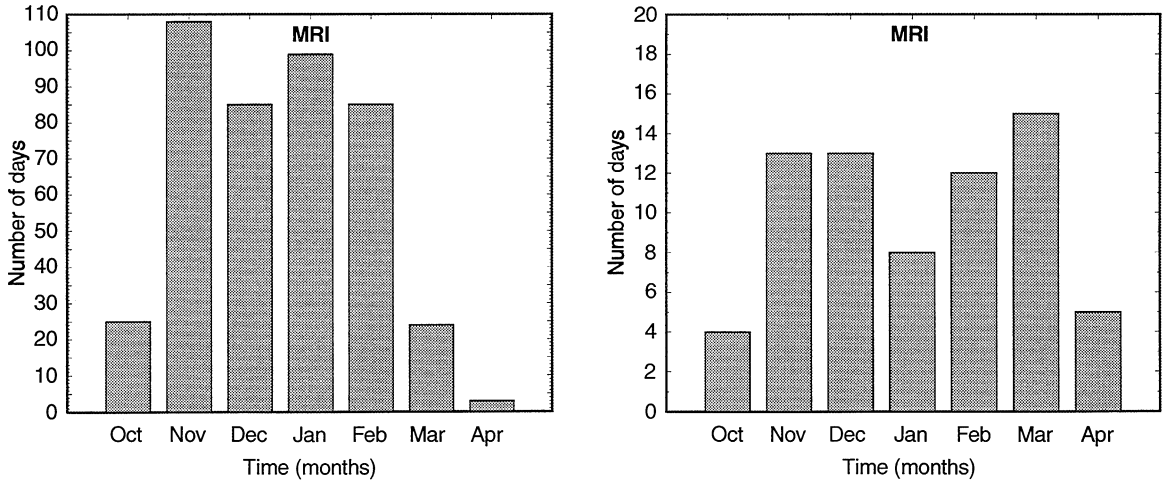

Fig. 7. (Continued)

the cold surges and the monsoon wind near Southeast Asia is pivotal to the coupling between the winter monsoon and the oceans.

Based on synoptic experience and previous study (Zhang et al. 1997), the northerly wind near southern China increases as the Siberian high intensifies. Once a cold surge outbreaks from the Siberian region, the maximum northerly wind propagates southeastward from southern China into the Taiwan area, and then penetrates further into the SCS and the maritime continent depending on its intensity.

We have computed the winter averaged correlation coefficient between region 1 SLP and region 3 meridional wind from all model simulations. The value of the correlation coefficient ranges from about -0.30 to -0.60. This is quite significant considering the degree of freedom of the samples (twice daily for nine winter seasons). Even for the lowest absolute value of the coefficient, the reversed phases between the region 1 SLP and region 3 meridional wind is visually obvious when the time series of the two are compared. This indicates that all models can simulate the connection between the Siberian high and the northerly wind near southern China.

Figure 8 shows the time series of surface meridional wind for region 3, near Taiwan, and near the SCS simulated from all the GCMs for the 1987/88 winter season, along with those from the reanalysis.

The reanalysis reveals the following: the patterns of temporal variation in all three regions are similar. The phases in southern China lead those near Taiwan, and the phases near Taiwan in turn lead those near the SCS. The phase difference between the variation patterns in each region, which represents the southeast propagation of the surface anticyclones, is $\sim$1–3 days. Another feature is that the meridional wind over the oceans is stronger than over the land. The magnitude of the meridional wind near Taiwan and the SCS is greater than that of the southern China land area. The wind drastically shifts from northerly to southerly during mid-March, suggesting the transition from winter to summer near the SCS. Throughout the winter, northerly wind dominates in all three regions, particularly near Taiwan and Hainan.

The models display a wide range of skill in reproducing the spatial and temporal variation of the meridional wind near this region. Note that apart from the CSIRO model, the range of the wind variation is bigger in the models than that in the reanalysis. This indicates that the majority of the models overestimate the amplitude of the meridional wind variation. Almost all the models reproduced the southeastward propagation of wind from southern China into the SCS, although in some there was a tendency for the wind to vary simultaneously at different regions. Most models were able to portray the difference in wind magnitude between the land and the oceans. In some models, however, the difference is ambiguous or no difference can be found. The most serious discrepancy occurs in the CSU model, where the northerlies over land are stronger than those over the oceans for a substantial period of time. The treatment of the boundary wind in the CSU model, as discussed already, is responsible for this discrepancy. As in the reanalyses, the simulated wind from most of the models is dominated by northerlies for most of the winter season. The sudden shift to southerly wind after March in several models suggests the ending of the subtropical winter monsoon. In the GFDL and the GLA models, however, episodes of strong southerlies occur during midwinter.

The reverse of the meridional wind, an important indicator of seasonal transition near the SCS, should be carefully examined in future studies, especially in the coupled simulations. The meridional wind characteristics near Southeast Asia may have important implications to ocean-atmosphere interaction during the spring transition season.

When the remaining years are considered, the skill of the model in simulating the wind characteristics in the three regions is consistent with what has been discussed. However, the wind displays interannual variation to different degrees depending upon the model. The observed interannual variation of the average meridional wind near

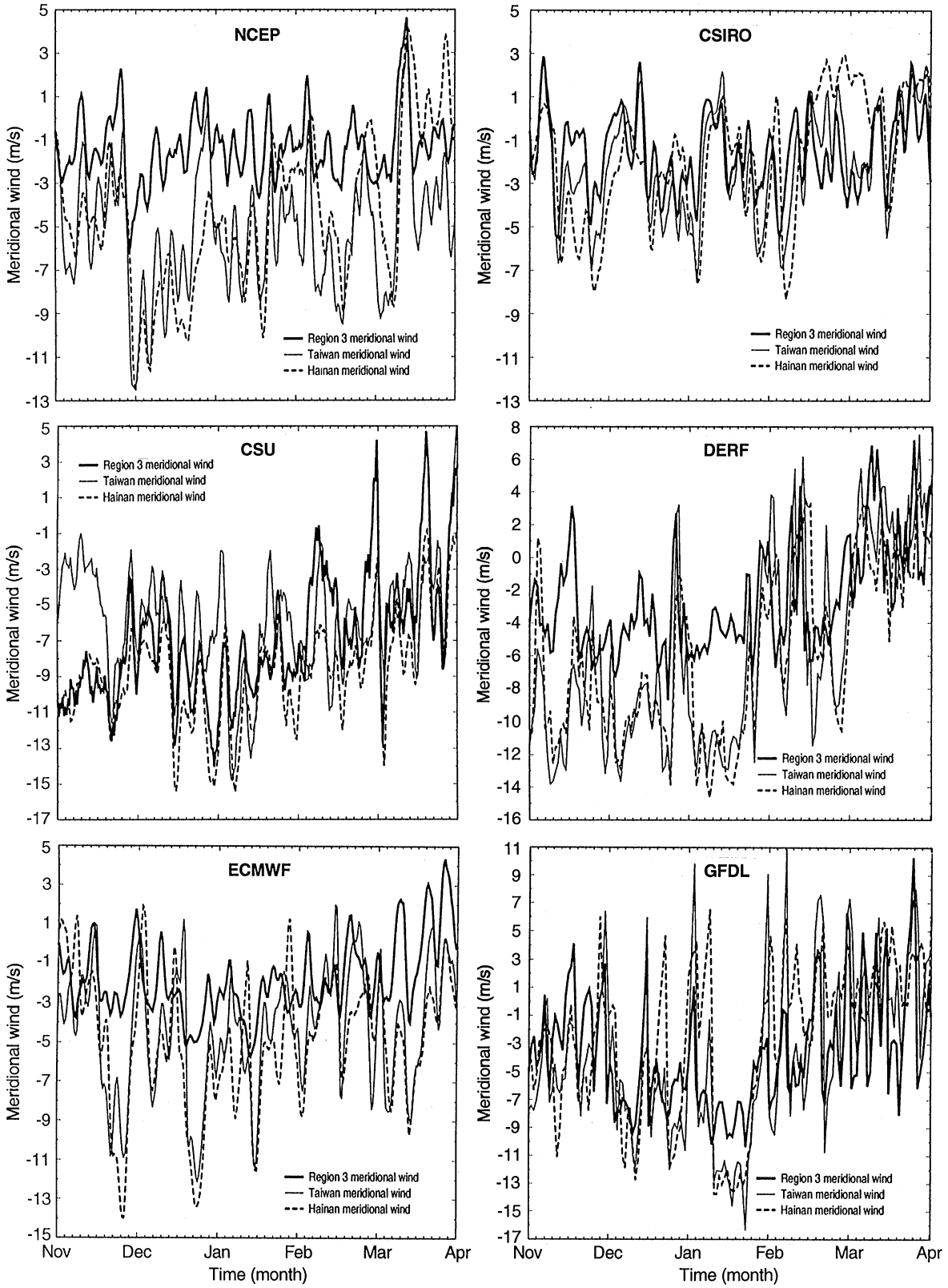

Fig. 8. Observed and model simulated twice daily time series of average meridional wind from region 3, near Taiwan (120 °E–125 °E; 22.5 °N–27.5 °N), and in the vicinity of the South China Sea (110 °E–115 °E, 10 °N–20 °N) from November of 1987 to March of 1988. A five-point running average has been applied to all the fields. Unit: $m\,s^{-1}$

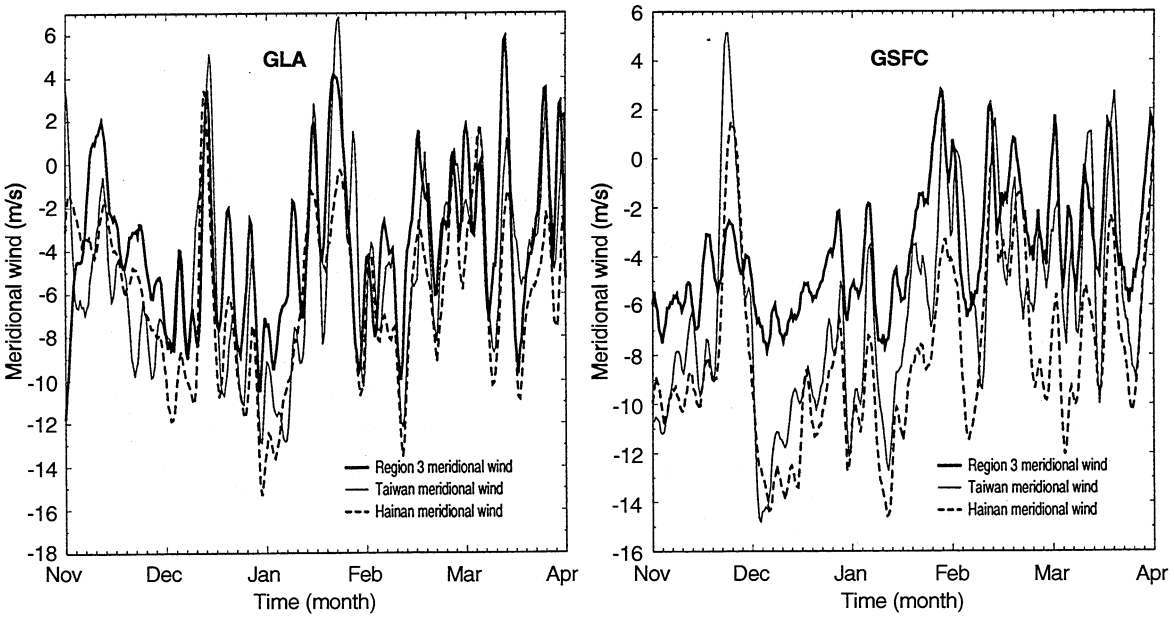

Fig. 8. (Continued)

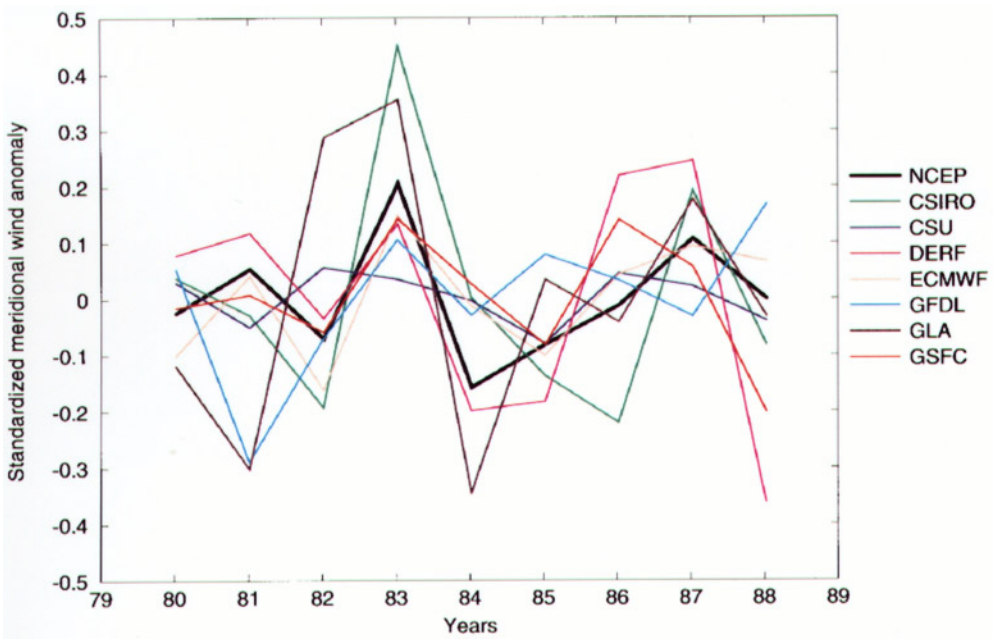

Fig. 9. Standardized winter (DJF) meridional wind anomaly near the South China Sea from the reanalysis and the models

the SCS (10 °N–20 °N, 110 °E–120 °E) is in good agreement with the SOI. Figure 9 presents the interannual variation of the standarized meridional wind anomaly averaged in the SCS region from the reanalysis and model simulations. During the 1982–83 El Nino event, most of the models were able to produce the weakened northerly winds. In the 1987–88 season, however, only about half of the models correctly simulated the wind minimum. In most of the model simulations, the interannual variation bears little resemblance to that from the observations with the exception of the CSIRO and ECMWF model, where good agreement was found.

Table 4 lists the correlation coefficient between the SOI and the wind near the SCS from models and the reanalysis. Except for the CSIRO and the ECMWF models, the relationship between the simulated wind variation and the SOI is not statistically significant. The magnitude ranges from 2.0 m/sec to 6.0 m/s with a consensus of 3.9 m/s, which is close to the reanalysis value.

Table 4. Correlation coefficient between the SOI and the interannual variation of the meridional wind near the South China Sea

	NCEP	CSIRO	CSU	DERF	ECMWF	GFDL	GLA	GSFC
R	− 0.89	− 0.94	− 0.25	− 0.44	− 0.75	− 0.18	− 0.48	− 0.55
v-wind (m/sec)	− 4.0	− 2.0	− 6.0	− 3.0	− 3.8	− 3.1	− 4.7	− 4.8

The forcing of cold surges on the tropical convection is also studied. Given that neither the observed convective precipitation nor the latent heat fluxes is available, the satellite observed daily outgoing longwave radiation (OLR) from the National Oceanic and Atmospheric Administration is used.

The convective activity on the time scale of surges is examined here. The correlation coefficient between daily Hainan meridional wind and OLR around Borneo (5 °S–10 °N, 110 °E–120 °E) is calculated. The magnitude of the coefficients ranges anywhere between 0.2 to 0.35 during different years of the AMIP decade (not shown). Despite the poor correlation, the strong cold surges (northerly wind greater than 10 m/s) are invariably related to abnormally low OLR, indicating that the deep convective activity becomes more extensive when a strong cold surge occurs. Similar relationship was found in Slingo (1997).

The relationship between the strong cold surges and the convection near Borneo is also studied in the models. The convective precipitation (or the total precipitation) is used instead of the OLR. For most of the models, the correlation coefficients between the Hainan meridional wind and the precipitation near Borneo are reversed relative to observation. Based on the current data, the strong events do not generally coincide with a precipitation peak in the models.

The poor relationship between the precipitation and strong cold surges may result from many factors. First, the total precipitation is used when the convective precipitation is not available. Even when the convective precipitation is available in the models, the precipitation can be influenced by other tropical phenomena, such as the Madden-Julian Oscillations. Second, the most dominant mode of the convection north of Borneo is that of a mesoscale rather than cumulus convective-scale (i.e., Houze et al. 1981; Johnson and Priegnitz 1981). The excitation of convection in the GCM may be affected if the interaction between the mesoscale circulation and cold surges is important in modulating the convection, simply because none of these GCMs can resolve mesoscale features. Finally, the response of the convection to the cold surge forcing may depend on the convective parametrization schemes used in the models. Also lack of a SST response to the cold surge forcing in the simulations can be a factor since SST is prescribed in the AMIP experiments.

Clearly, the cold surge forcing on the tropical convection needs to be further studied with high quality observations and more complete model output.

5 Summary and conclusions

This study has evaluated the simulation of the East Asian winter monsoon by eight atmospheric GCMs that participated in the AMIP. The models are able to portray the observed mean state of the monsoon circulation. In most of the GCMs, the locations of the Siberian high and the neighboring Aleutian low are in reasonable agreement with respect to the reanalysis. Except for a few models, the intensity of the central pressure is simulated to within approximately 5 hPa relative to the reanalysis. The anticyclonic surface wind near the Siberian region and the maximum northeasterlies near the SCS are realistically reproduced in most of the models. The magnitude of the wind, however, varies between models. Some overestimate or underestimate the wind magnitude by approximately 50% depending on the region. The velocity potential minimum near the maritime continent is satisfactorily simulated, as is the zonal wind configuration near the 200 hPa jet stream. However, none of the models were able to reproduce the gradient of the velocity potential near the southeast coast of China as strong as in the reanalysis. In some of the models this is directly related to the southeastward displacement of the convection center. The improper location of the convection results in a weak gradient of the velocity potential near Southeast Asia, which in turn reduces the jet intensity at the 200 hPa.

Models display a wide range of skill in simulating the cold surges and their transient properties. The transient temperature variations associated with the cold surges typically fall within the observed range, although some models tend to moderately overestimate or underestimate the temperature range. The southward propagation of surge-related temperature pulses from the Siberian region toward southern China are realistically simulated from all the models. Most of the models tend to underestimate the cold surge frequency. The simulated cold surge intensity measured by the pressure at the anticyclone center is close to that from the reanalysis. Although the source regions of the cold air are not satisfactorily simulated, the observed cold-surge trajectories have been reproduced in most models. The simulated evolution patterns of the cold surge associated SLP, surface air temperature and surface meridional wind agree with the observation to various degrees.

It is somewhat surprising that most models are able to reproduce the temporal variation of the cold surges and the Siberian high. The peak frequency in November and March requires the realistic representation of both the thermodynamical and the dynamical characteristics of the atmosphere near the East Asian region.

Most GCMs were able to simulate the link between the cold surges and the tropical surface wind, although a few models generated unrealistic subtropical southerly wind during the mid-winter. The forcing on the tropical convection is also analyzed. Due to the lack of some required variables in the model output, the results are not

conclusive. Most GCMs have difficulty in reproducing the detailed aspect of observed forcing pattern of cold surges. This is because many potentially important mechanisms affecting the convection cannot be adequately delineated in the GCMs. Observational studies related to the forcing of cold surges on the tropical convection are much needed when high quality data become available.

The satisfactory simulations of the mean monsoon circulation and the evolution of the cold surges can be partly attributed to the topographical and geographical characteristics of the East Asian continent, although some surge characteristics are not related to the Tibetan Plateau (Nakamura and Murakami (1983). The orientation and height of the Tibetan Plateau greatly affect the formation of the Siberian cold dome, the surface wind, the pressure field. Once the cold surges outbreak from this region, they are forced by the high terrain to propagate southeastward along the eastern edge of the Plateau. The cold surges that reach the oceans are strongly dissipated by the warm and moist marine boundary-layer. Therefore, the oceans to the east of the continent restrict the eastward extent of the propagation. The rest of the cold surges propagate further south, and some penetrate into the SCS region.

The discrepancies in the simulations can result from many factors. The most prominent ones are the improper position of the convective center, which is likely related to the cumulus parametrization schemes in some models.

Studies have suggested that the interaction between the tropical convection and the mid-latitude circulation is critically dependent upon the relative position of the convection and the extratropical quasi-stationary waves (Branstator 1983). The relative position of the convective center and the Siberian high can be favorable or unfavorable for the southward penetration of the cold surges. Therefore, the correct positioning of the mean monsoon circulation is important for the description of the transient behavior of cold surges. If the models cannot correctly simulate the mean position of the tropical convection, other planetary features will not be accurately reproduced. These will include the magnitude of the ageostrophic wind, intensity of the local Hadley cell, the jet stream and the mean baroclinicity of the atmosphere. On the other hand, the feedback to the planetary scale circulation resulting from the interaction between cold surges and tropical disturbances will most likely deviate the circulation further away from the observed pattern, if the intensity and location of the convection and the mean circulation were not correctly simulated in the first place.

While the most obvious culprits for the discrepancies in the monsoon simulations appear to be improper locations of the western Pacific convection centers, other aspects may also be important in affecting the simulations, but they are very difficult to quantify. For example, Ding (1996, personal communication) has found that the *dry* and *cold* air associated with the surge of high pressure frequently interacts with the *moist* and *warm* air associated with troughs that moving out of the Bay of Bengal, and the interaction results in changes in the characteristics of surges and tropical circulations near the surface. The simulation of this phenomenon may be a taxing job for most of the GCMs. Tests using a case study approach from output of high-resolution models may provide important clues concerning the simulation of this synoptic-scale interactions.

Once the cold surges arrive in the SCS area, the air-sea interaction can further increase the low-level northeasterly wind and intensify the organized deep cumulus convection (Ding 1994; Chang et al. 1979). In some cases, the reduced SST due to the cold air incursion will stabilize the atmosphere and weaken the convection (Chang et al. 1979). In the AMIP simulations, the observed convective characteristics and wind fluctuations that are greatly affected by the air-sea interactions will not be present given that the SST is prescribed.

The correct simulation of the interannual variation of the surface wind near the SCS is a demanding task for most of the GCMs. This requires adequate simulations of many features, including the extratropical surface pressure systems, the tropical convection, the tropical and extratropical linkage and air-sea interactions near the maritime continent. Despite this, the CSIRO and ECMWF models were able to reproduce the observed interannual variation of meridional wind over the SCS. There are certain agreements among different models and observations during the 1981/82, 1983/84, and 1986/87 season. During the 1982/83 season when the strong SST signal is the dominant factor, all the models correctly simulated the wind minimum. However, the agreement is not as good during the rest of the years when many other factors may also contribute to the wind variation. One of the most important among them is, quite likely, the interaction between the oceans and the winter monsoon.

The simulated errors noted from this study furnish a guide for the continuing improvement of the winter monsoon simulations. With more realistic representations on various aspects of the winter monsoon, the AGCMs will possess better skill in reproducing the observed surface wind and its interannual variation near Southeast Asia, and have better skill in delineating the convective activities near the western Pacific. Such skill is not only important for simulating the air-sea interaction in the boreal spring transition season, but also critical for portraying the winter monsoon forcing and the monsoon/ENSO interactions in a coupled model.

Acknowledgements. Special thanks to NCEP/NCAR for making the reanalysis data available. The invaluable comments and critiques provided by Lydia Dumenil and Mark Heer are greatly appreciated. Michael Fiorino helped with the NCEP/NCAR reanalysis and GrADS. This work was performed under the auspices of the US Department of Energy Environmental Science Division at the Lawrence Livermore National Laboratory under contract W-7405-ENG-48.

References

Barnett TP, Dumenil L, Schlese U, Roeckner E, and Latif M (1989) The effect of Eurasian snow cover on regional and global climate variations. J Atmos Sci 46:661–685

Boyle JS (1986) Comparison of the synoptic conditions in midlatitude accompanying cold surges over the Eastern Asia for the months of December 1974 and 1978. Part 1: monthly mean fields and individual events. Mon Weather Rev 114:903–918

Boyle JS, Chen TJ (1987) Synoptic aspects of the wintertime East Asian monsoon. In: Chang C-P, Krishnamurti, TN (eds) Monsoon meteorology. Oxford University Press, pp 125–160

Branstator G (1983) Horizontal energy propagation in a barotropic atmosphere with meridional and zonal structure. J Atmos Sci 40:1689–1708

Chang CP, Lau KM (1980) Northeasterly cold surges and near-equatorial disturbances over the Winter MONEX area during December 1974. Part 2: planetary-scale aspects. Mon Weather Rev 108:298–312

Chang CP, Lau KM (1981) Planetary-scale motions of winter monsoons during cold surges and break periods. Proc Int Conf on early results of FGGE and large-scale aspects of its monsoon experiments. Tallahassee, FL, World Meteorological Organization, pp 12–19

Chang CP, Lau KM (1982) Short-term planetary scale interaction over the tropics and the mid-latitudes. Part 1: contrast between active and inactive period. Mon Weather Rev 110:933–946

Chang CP, Erickson J, Lau KM (1979) Northeasterly cold surges and near-equatorial disturbances over the winter-MONEX area during 1974. Part 1: synoptic aspects, Mon Weather Rev 107:812–829

Chu PC, Huang MJ, Fu EX (1996) Formation of the South China Sea warm-core eddy in boreal spring. Proc AMS Conf Global Ocean-Atmosphere-Land System (GOALS), Atlanta, Georgia, pp 155–159

Davidson NE, McBride JL, McAvaney BJ, (1983) The onset of the Australian monsoon during Winter MONEX: synoptic aspects. Mon Weather Rev 111:495–516

Ding YH (1994) Monsoon over China. Kluwer Academic Publishers, 432 pp

Ding YH, Krishnamurti TN (1987) Heat budget of the Siberian high and the winter monsoon. Mon Weather Rev 115:2428–2449

Gates WL (1992) AMIP: The Atmospheric Model Intercomparison Project. Bull Am Meteorol Soc 73:1962–1970

Houze RA, Geotis SG, Marcks FD, West AK (1981) Winter monsoon convection in the vicinity of north Borneo. Part 1: structure and time variation of the clouds and precipitation. Mon Weather Rev 109:1595–1614

Johnson RH, Priegnitz DL (1981) Winter monsoon convection in the vicinity of north Borneo. Part 2: effects on large-scale fields. Mon Weather Rev 109:1615–1628

Ju JH, Slingo JM (1995) The Asian summer monsoon and ENSO. Qt J R Meteorol Soc 121:1133–1168

Kalnay E, Kanamitsu M, Kistler R, Collins W, Deaven D, Gandin L, Iredell M, Saha S, White G, Wollen J, Zhu Y, Chelliah M, Ebisuzaki W, Higgins W, Janowiak J, Mo KC, Ropelewski C, Wang J, Leetmaa A, Reynolds R, Jenne R, Joseph D (1996) The NCEP/NCAR 40-year reanalyses project. Bull Am Meteorol Soc 77:437–471

Lau KM, Chang CP (1987) Planetary scale aspects of the winter monsoon and atmospheric teleconnections. In: Chang C-P Krishnamurti TN (eds) Monsoon meteorology, Oxford University press, pp 161–201

Li CY (1990) Interaction between anomalous winter monsoon in East Asia and El Nino Events. Adv Atmos Sci 7:36–46

Luo HB (1995) Effect of winter monsoon on summer monsoon through air-sea interaction. Acta Meteorol Sinica 9:26–34

Luo SW (1992) Weather systems near the Tibetan Plateau. Chinese Meteorological Press. 201 pp (in Chinese)

Meehl GA (1994) Influence of the land surface in the Asian summer monsoon: external conditions versus internal feedbacks. J Clim 7:1033–1049

Murakami T (1987) Effects of the Tibetan Plateau. In: Chang C-P Krishnamurti TN (eds) Monsoon meteorology, Oxford University press, pp 235–270

Nakamura H, Murakami T (1983) Orographic effects on cold surges and lee-cyclogenesis revealed by a numerical experiment. Part 1 Time mean aspects. J Meteorol Soc Japan 61:524–546

Phillips TJ (1994) A summary documentation of the AMIP models. PCMDI Report 18, PCMDI, Lawrence Livermore National Laboratory, Livermore, California 94550

Shield K (1985) Possible cross-equatorial influences of the northeast monsoons on the onset of the Indonesian westerly monsoon. Master Thesis, Naval Postgraduate School. (Available form Prof. C-P Chang, Naval Postgraduate School, Monterey, CA, 93943)

Slingo JM (1997) Extratropical forcing of tropical convection in a northern winter simulation with the UGAMP GCM, Q J R Meteorol Soc (in press)

Sperber KR, Palmer TN (1996) Interannual tropical rainfall variability in general circulation model simulations associated with the atmospheric model intercomparison project. J Clim 9: 2727–2750

Sperber KR, Hameed S, Potter GL, Boyle JS (1994) Simulation of the southern summer monsoon in the ECMWF model: sensitivity to horizontal resolution. Mon Weather Rev 122:2461–2481

Sperber KR, Slingo JM, Inness PM, Lau KM (1997) On the maintenance and initiation of the interseasonal oscillation in the NCEP/NCAR reanalysis and the GLA and UKMO AMIP simulations. Clim Dyn 13: 769–795

Staff members, Academia Sinica 1958: On the general circulation over eastern Asia. Tellus 10:58–75

Sun SQ, Sun BM (1996) The relationship between the anomalous winter monsoon circulation over East Asia and summer drought/flooding in the Yangtze and Huaihe river in China. Proc 3rd Conf East Asia and Western Pacific Meteorology and Climate. National Central University, Chung-Li, Taiwan, pp 115–120

Takacs LL, Suarez MJ (1996) Dynamical aspects of climate simulations using the GEOS general circulation model. NASA Techn Mem 104606, 10:56pp

Tomita T, Yasunari T (1996) Role of the northeast winter monsoon on the biennial oscillation of the ENSO/Monsoon system. J Meterol Soc Japan 74:399–413

Webster PJ, Yang S (1992) Monsoon and ENSO: Selectively interactive systems. Q J R Meteorol Soc 118:877–926

Yeh TC, Gao YX (1979) Meteorology of the Tibetan Plateau: Scientific Publication Agency, Beijing, 304pp (in Chinese)

Zhang Y, Wang WC (1997) GCM simulated northern winter cyclone and anticyclone activity under a greenhouse warming scenario. J Clim 10:1616–1634

Zhang Y, Sperber KR, Boyle JS (1997) Climatology and interannual variation of East Asian winter monsoon: results from the 1979–1995 NCEP/NCAR reanalysis. Mon Weather Rev (in press)

Zhou FX, Yu SY, Fu G, Wang DX (1996) The oscillations of meridional sea level wind in the South China Sea and its impact on sea surface temperature. Proc 3rd Conf East Asia and Western Pacific Meteorology and Climate. National Central University, Chung-Li, Taiwan, pp 359–362